

AUTOMATED FARM FIELD DELINEATION AND CROP ROW DETECTION FROM SATELLITE IMAGES

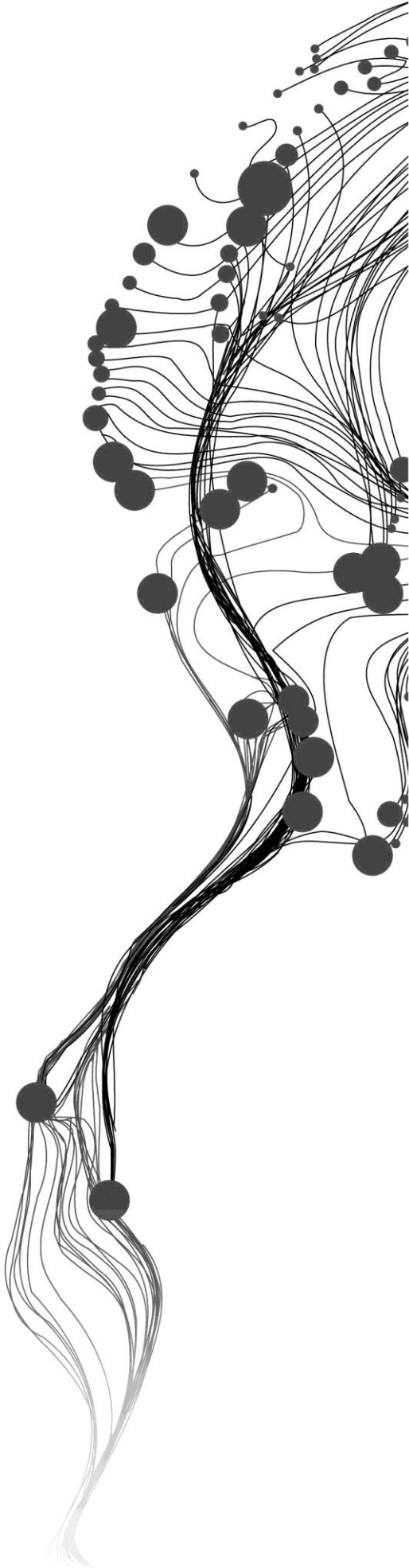
MELKAMU MESERET ALEMU

February, 2016

SUPERVISORS:

Dr. Valentyn Tolpekin

Dr.ir. Wietske Bijker



AUTOMATED FARM FIELD DELINEATION AND CROP ROW DETECTION FROM SATELLITE IMAGES

MELKAMU MESERET ALEMU

Enschede, The Netherlands, February, 2016

Thesis submitted to the Faculty of Geo-Information Science and Earth Observation of the University of Twente in partial fulfilment of the requirements for the degree of Master of Science in Geo-information Science and Earth Observation.

Specialization: Geoinformatics

SUPERVISORS:

Dr. Valentyn Tolpekin

Dr.Ir. Wietske Bijker

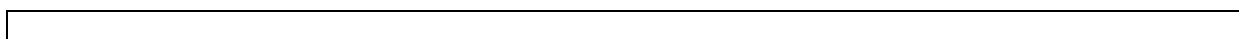
THESIS ASSESSMENT BOARD:

Prof.Dr.Ir. A. Stein (Chair)

Dr. I.C. van Duren (External Examiner, University of Twente, ITC-NRS)

DISCLAIMER

This document describes work undertaken as part of a programme of study at the Faculty of Geo-Information Science and Earth Observation of the University of Twente. All views and opinions expressed therein remain the sole responsibility of the author, and do not necessarily represent those of the Faculty.



ABSTRACT

Agriculture is vital to the food security and economic growth of most countries in the world, especially in developing countries. Accurate information on field boundaries has considerable importance in precision agriculture and greatly assists land administration systems. The information obtained from field boundaries can provide valuable input for agricultural applications like crop monitoring and yield predictions.

Farm field information extraction is an important task and is highly related to food security. Farm field boundaries can be delineated by conventional field surveying methods or by digitizing satellite imagery manually. However, this approach is time consuming, costly and highly dependent on the operator's capability of digitization and interpretation. Low and medium resolution satellite images have limited capacity to offer accurate information for field level. But, very high resolution satellite images can provide farm field information accurately to sub-meter level, though extracting the required information from them is a big challenge due to the complex ground environment.

In this research, the capability of the line segment detection (LSD) algorithm for extracting linear features is explored on two real applications in the agricultural sector: field boundary delineation and crop rows detection from very high resolution satellite images. The algorithm starts by calculating the level-line angle for each pixel based on pixel gradient. As LSD is taking only a single band as an input, in order to concentrate all the available information, the gradient information in all bands is combined as a single band by taking the vector sum of image gradients in all bands. The level-line angle is used to form the line-support region, potential candidates for a segment, and is validated by Helmholtz principle based on NFA calculation. In addition to image bands, texture bands were explored. The effects of different second order GLCM texture measures on the results of LSD were examined.

In this research, validation method was developed. The optimum values of the three internal parameters of LSD for the purpose of field boundary delineation were $S = 1.0$, $\tau = 22.5^\circ$ and $\epsilon = 1.0$. Similarly, the optimum values these parameters for crop rows detection were $S = 0.8$, $\tau=22.5^\circ$ and $\epsilon =1.0$. These optimum parameter values agree with the ones proposed by Grompone von Gioi et al. (2012) except some difference on the scale parameter for the first application.

Accuracy assessment was performed following the proposed method by defining the two error ratios: the ratio of missing detection and the ratio false detection. The results obtained for the first application (field boundary delineation) are $RM=0.78$ and $RF= 0.73$. The results for the second application (crop rows detection) are $RM =0.17$ and $RF=0.48$.

In this research, the different approaches followed: extracting information from multiple bands, using texture bands or image bands in detecting field boundaries do not give good results. On the other hand, the results obtained from the crop rows detection show that the adopted methodology has a good potential in detecting crop rows as well as their dominant orientations.

ACKNOWLEDGEMENTS

I would like to express my heartfelt appreciation to my supervisors Dr. Valentyn Tolpekin and Dr. Ir. Wietske Bijker for their continued support, guidance, encouragement, immense knowledge and for their patience. I have indeed learnt a lot from them.

I sincerely thank Dafni Sidiropoulou Velidou for allowing me to use part of the LSD R code.

I am also grateful to all Staff members of ITC who in one way or another involved in my learning process and to the Netherlands Fellowship Programmes (NFP) for awarding me the scholarship that made my studies possible at ITC.

I would like to thank my family for their love, steady encouragement and support. To my brother Workineh Meseret and sisters Desta and Mahlet Meseret thank you for everything. To Yenework Mulualem I have no words to say but thank you for your patience and understanding.

Lastly, I heartily thank all Habesha community at ITC for making my stay at ITC enjoyable and memorable.

Melkamu Meseret Alemu
February, 2016

TABLE OF CONTENTS

Abstract	i
Acknowledgements	ii
List of figures	v
List of tables	vii
1. Introduction	1
1.1. Problem statement	1
1.2. Background	3
1.3. Research Identification	4
1.3.1. Research Objective	4
1.3.2. Research Questions	4
1.4. Innovation aimed at	5
1.5. Method adopted	5
1.6. Outline of the thesis	7
2. Literature Review	9
2.1. Boundary concepts	9
2.2. Gestalt theory and The Helmholtz principle	9
2.3. Texture information for image segmentation and boundary mapping	10
2.4. Related works	10
2.5. Accuracy Assessment	12
3. Data	13
3.1. Study area	13
3.2. Imagery and Reference data	14
3.2.1. Very High Resolution Satellite image	14
3.2.2. Reference data	14
3.3. Software	14
4. Methodology	15
4.1. Texture calculation	15
4.1.1. GLCM contrast	16
4.1.2. GLCM dissimilarity	16
4.1.3. GLCM homogeneity	16
4.1.4. GLCM entropy	16
4.1.5. GLCM angular second moment (ASM) and energy	16
4.1.6. GLCM mean	16
4.1.7. GLCM variance	16
4.1.8. GLCM correlation	16
4.2. Line Segment Detection Algorithm	17
4.2.1. Multispectral analysis	18
4.2.2. Image scaling	18
4.2.3. Gradient computation	18
4.2.4. Gradient ordering and threshold	20
4.2.5. Region Growing	20
4.2.6. Line segment localization	21
4.2.7. Rectangular approximation	22
4.2.8. Number of False Alarms (NFA) computation	23

4.3.	Crop rows detection.....	24
4.4.	Parameter tuning and validation	25
4.4.1.	Edge Strength Determination.....	25
4.4.2.	Validation and Accuracy Assessment.....	27
4.4.3.	Parameter tuning.....	28
5.	Results	29
5.1.	Farm field delineation	29
5.1.1.	Tuning of S.....	29
5.1.2.	Tuning of gradient magnitude threshold ρ	32
5.1.3.	Tuning of angle tolerance.....	33
5.1.4.	Tuning of detection threshold epsilon (ϵ)	35
5.2.	Parameter tuning for crop rows detection	39
5.2.1.	Tuning of S.....	39
5.2.2.	Tuning of τ	42
5.2.3.	Tuning of detection threshold ϵ	43
5.3.	Validation of the results of crop rows detection	45
5.4.	Dominant orientation of crop rows.....	48
5.5.	Spacing of Crop rows	50
6.	Discussion.....	51
6.1.	Field boundary delineation	51
6.2.	Crop rows detection.....	52
7.	Conclusions and recommendations.....	53
7.1.	Optimal parameter setting	53
7.2.	Assessment of the detection results	53
7.2.1.	Field boundary delineation.....	53
7.2.2.	Crop rows detection.....	53
7.3.	Recommendations.....	54
	List of references	55
	Appendix	60

LIST OF FIGURES

Figure 1.1: Flowchart of the methodology.....	6
Figure 3.1: Study area.....	13
Figure 4.1: The four directions for calculating texture features.....	15
Figure 4.2: (a) Example of input image with 4 grey levels (b) GLC M for distance $d = 1$ and direction 0°	15
Figure 4.3: Gradient computation using 2×2 mask.....	19
Figure 4.4: Image gradient. (a) Horizontal direction, (b) Vertical direction.....	19
Figure 4.5: Edge orientation, reprinted from Meer and Georgescu (2001).....	20
Figure 4.6: Regional growing process of aligned points, reprinted from Morel et al. (2010).....	21
Figure 4.7: Representation of a line by ρ and θ	22
Figure 4.8: Example of a line-support region and its associated line segment.....	22
Figure 4.9: The smallest rectangle that covers all pixels of the line-support region: (a) without line segment. (b) with line segment.....	23
Figure 4.10: Rotating the lines by angle θ to make them parallel to the x-axis, d is the spacing between the lines.....	24
Figure 4.11: Line- support region W with its corresponding line that divides the region into $R1$ and $R2$	25
Figure 4.12: Steps in edge strength determination.....	26
Figure 5.1(a) Ratio of missing(RM) and ratio of false (RF) detections, (b) RM+RF for varying scale parameter S for fixed $\tau = 22.5^\circ$ and $\varepsilon = 1$. The low S value would imply coarse spatial resolution and large S value would imply fine spatial resolution.....	30
Figure 5.2: Detection results for different S values. (a) $S = 0.2$, (b) $S = 0.5$, (c) $S = 0.8$, (d) $S = 1.0$. Blue segments: reference segments, white: detected segments. For the image displayed: $R = 7$, $G = 5$, $B = 3$	30
Figure 5.3: Distance between points for varying the value of S	31
Figure 5.4: Box plots showing distributions of contrast and steepness of true detections and false detections. (a) Contrast of successful detections, (b) Contrast of false detections, (c) Steepness of true detections, (d) Steepness of false detections.....	32
Figure 5.5 (a) Ratio of missing (RM) and ratio of false (RF) detections, (b) RM+RF for varying τ for fixed $S = 1.0$ and $\varepsilon = 1.0$	33
Figure 5.6: Detection results for different τ values for fixed values $S = 1.0$, $\varepsilon = 1.0$ (a) $\tau = 10^\circ$, (b) $\tau = 17.5^\circ$, (c) $\tau = 22.5^\circ$, (d) $\tau = 25^\circ$. Blue segments are reference segments, white segments are detected segments. For image displayed $R=7$, $G=5$, $B=3$	34
Figure 5.7: Detected line segments with reference dataset on image band(blue segments are reference segments, white segments are detected segments, $R=7$, $G=5$, $B=3$) for $S=1$, $\tau=22.5^\circ$ and $\varepsilon=1$	36
Figure 5.8: Successful detections from reference to detection for $S=1$, $\tau = 22.5^\circ$, $\varepsilon = 1$. Blue segments are reference segments, black segments are detected segments, green segments show successful detections.....	36
Figure 5.9: Successful detections from detection to reference for $S=1$, $\tau=22.5^\circ$, $\varepsilon=1$. Blue segments are reference segments, red segments are detected segments, green segments show successful detections.....	37
Figure 5.10: RM and RF for three spatial distance values in the horizontal direction. (a) GLCM contrast, (b) GLCM mean, (c) GLCM variance.....	38
Figure 5.11: Detected line segments with reference dataset on texture band (GLCM contrast for $d = 3$ in the horizontal direction) for $S=1$, $\tau = 22.5^\circ$, $\varepsilon = 1$. Blue segments are reference segments, white segments are detected segments, $R=7$, $G=5$, $B=3$	38

Figure 5.12 (a) Ratio of missing(RM) and ratio of false(RF) detections, (b) RM+RF for varying scale parameter S for fixed $\tau = 22.5^\circ$ and $\epsilon = 1$. The low S value would imply coarse spatial resolution and large S value would imply fine spatial resolution. An optimum value is observed at $S = 0.8$	40
Figure 5.13: Successful detections for two different S values. Green: successful detection. (a) Successful detections from reference to detection for $S = 0.5$, (b) Successful detections from detection to reference for $S = 0.5$, (c) Successful detections from reference to detection for $S = 0.8$, (d) Successful detections from detection to reference for $S = 0.8$. Detection results are better for (c) and (d) than (a) and (b). which shows the influence of scale parameter on detection results.....	41
Figure 5.14: (a) Ratio of missing(RM) and ratio of false(RF) detections, (b) RM+RF for varying angle tolerance τ . Low τ values are more restrictive for region growing, which does not allow pixels with large differences in gradient orientation to be included in the same line-support region.	42
Figure 5.15: Detected results for optimum parameter values $S=0.8$, $\tau = 22.5^\circ$ and $\epsilon = 1$	43
Figure 5.16: Successful detections from reference to detection for optimum parameter values $S=0.8$, $\tau=22.5^\circ$ and $\epsilon = 1$. Green color shows successful detections, red color shows missed detections, black lines are detected rows.....	44
Figure 5.17: Successful detections from detection to reference for optimum parameter values $S = 0.8$, $\tau = 22.5^\circ$ and $\epsilon = 1$. Green line segments show successful detections, red line segments show false detections.....	44
Figure 5.18: Results of Subset 1 for optimum parameter values $S=0.8$, $\tau=22.5^\circ$ and $\epsilon=1$. (a) Detected results, (b) Successful detections from reference to detection, (c) Successful detections from detection to reference.....	46
Figure 5.19: Results of Subset 4 for optimum parameter values $S=0.8$, $\tau=22.5^\circ$ and $\epsilon=1$. (a) Detected results, (b) Successful detections from reference to detection, (c) Successful detections from detection to reference	47
Figure 5.20: Detected results for optimum parameter values $S=0.8$, $\tau=22.5^\circ$ and $\epsilon=1$ of a field with no crop rows. No detection was reported in the field except near the boundaries of the field.....	48
Figure 5.21: Rose diagram of dominant orientation of crop rows of both reference and detection for four validation subsets. (a-d) are the orientations of reference rows and (e-h) are the orientations of their corresponding detected rows of subsets 1-4 respectively.....	49
Figure 5.22: Row spacing of four subsets. (a) Subset 1, (b) tuning subset, (c) subset 3, (d) subset 4. The vertical lines indicate the lags at which dominant frequencies are found.	50

LIST OF TABLES

Table 3.1: WorldView-2 satellite image specifications.....	14
Table 5.1: RM and RF for varying S for fixed $\epsilon = 1$ and $\tau = 22.5^\circ$	29
Table 5.2: RM and RF for varying gradient magnitude threshold for fixed $S = 1$, $\tau = 22.5^\circ$ and $\epsilon = 1$	32
Table 5.3: RM, RF, Average distance and standard deviation between corresponding points for varying τ for fixed $S = 1$, $\tau = 0$ and $\epsilon = 1$	33
Table 5.4: RM and RF for varying detection threshold ϵ for fixed $S = 1.0$ and $\tau = 22.5^\circ$	35
Table 5.5: RM and RF for three spatial distance values.....	37
Table 5.6: RM and RF for varying S for fixed $\tau = 22.5^\circ$ and $\epsilon = 1$	39
Table 5.7: RM and RF for varying angle tolerance τ and for fixed values of $S = 0.8$ and $\epsilon = 1$	42
Table 5.8: RM and RF for varying detection threshold ϵ and for fixed values of $S = 0.8$ and $\tau = 22.5^\circ$	43
Table 5.9: RM and RF for different subsets for optimum parameter values $S = 0.8$, $\tau = 22.5^\circ$ and $\epsilon = 1$	45
Table 5.10: Dominant orientation of crop rows and number of rows.....	48
Table 5.11: Spacing of crop rows for four subsets.....	50

1. INTRODUCTION

1.1. Problem statement

Agriculture is vital to the food security and economic growth of most countries in the world, especially in developing countries. African economies depend heavily on agriculture and the agriculture provides a large share of the gross domestic product (GDP) in some sub-Saharan African countries (AGRA, 2013). Most farming in Africa is carried out by smallholders using traditional techniques. These smallholders contribute up to 90% of the nations' staple food production (Jain et al., 2013) by using traditional farming practices. They do not have access to modern agriculture knowledge and techniques. Though agriculture contributes a large share to GDP, most African countries are self-insufficient in food. Alleviating food insecurity and ensuring sustainable development in the region is one of the top agenda that seeks attention. Proper management of land resources is the basis for sustainable development and is directly related to agricultural development and food security (Dekker, 2001). To manage land resources effectively, there is a need for reliable, accurate and up to date information system about land. The main aim of land administration systems is to improve tenure security and access to land (Lengoiboni et al., 2011). However, land administration systems and proper management policies remain a challenge to most African countries (Kurwakumire, 2014). Depending on development stage of the economy and land tenure (mode of holding or occupying land) arrangements, land administration faces many challenges (Bogaerts & Zevenbergen, 2001). The lack of transparent land tenure information systems severely limits the engagement of smallholders, communities and investors in sustainable investment in land resources and generates social instability through land disputes. Tenure security provides community and investor confidence in development planning, land-based economic growth, natural resource management and environment sustainability and social stability (Donnelly, 2012). The core of land administration and tenure security is agreements on location of property boundaries. The interpretation of the location of these boundaries can be difficult and judgments may vary depending on the interpretation of the evidence of the location (Donnelly, 2012). Accurate information on field boundary has considerable importance in precision agriculture and greatly assists land administration systems. Therefore, it is important to find affordable technologies and efficient methods that assist decision making and effective use of land resources. Modern technologies, such as remote sensing and spatial information systems are revolutionizing agriculture. However, the use of these technologies is still far in Africa due to the heterogeneous nature of the agriculture, differences in crop cycles, the spatial heterogeneity of landscape, small and ill-defined farm fields, data accessibility issues, especially for high resolution data. This challenge has a negative impact on the proper planning, monitoring and effective utilization of land resources for sustainable development of the region. Thus, research based agricultural innovations, high precision and low cost technologies and suitable information extraction methods that can be easily applied in the region are essential to overcome challenges. To this end, The Spurring a Transformation for Agriculture through Remote Sensing (STARS) project, a research project looking for ways how remote sensing technology can help to improve agricultural practices and advance the livelihoods of smallholder in Sub-Saharan Africa and South Asia, is working to overcome the barriers and challenges of agricultural practices and land management related issues by finding evidence-based solutions sustainably so that smallholders, the farming community and decision makers can benefit out of it.

Agricultural applications (like crop row identification, crop protection and yield estimation) of remote sensing technology require quantitative analysis of remotely sensed data with high accuracy and reliability (Ferencz et al., 2004) and these can be achieved better on a field level. But, the definitions of the words 'field' and 'boundary' are context dependent. So, the fundamental unit of land that shares a certain property (parcel) need to be defined and identified. The parcel is described by its boundaries. Delineation of farm field boundaries is an important task to provide reliable information for monitoring farm fields and for yield prediction. Such predictions are crucial for field-level planning and site specific recommendations. Many information extraction techniques (surveys) have been used to delineate field boundaries. Generally, these methods can be grouped into three parts: ground based surveying, aerial surveys and satellite based surveying (Ali et al., 2012). Ground based surveying methods are conducted by surveyors using different surveying techniques and instruments like optical square, plane tabling etc. Nowadays, Global Positioning System (GPS) is broadly used to locate the position of points on the ground. Ground based survey is quite accurate, but labor intensive, sometimes requires an enormous amount of time and resources, including a number of skilled surveyors for large area application. On the other hand, aerial survey from aerial photogrammetry offers cost effective and time saving means of information extraction for land surveying and mapping. Moreover, aerial survey offers richer data than ground survey vector data (Barry & Coakley, 2013). Although the aerial survey is a better alternative to ground based survey, it is highly dependent on weather and climatic conditions (Ali et al., 2012). Sometimes, it is also impossible to undertake aerial surveys in some regions due restrictions for military security reasons. Satellite based surveying is the other method which offers many of the required spatial inputs for land surveying in digital form. As compared to aerial surveying, satellite based surveying covers a wide area more repeatedly and economically (Ali et al., 2012). Moreover, because of increasing spatial resolution satellite imagery is becoming more and more a viable alternative to aerial photographs.

Linear features extracted from remotely sensed data are important data sources for geospatial information analysis. Edges in the remote sensing image describe the structural information of linear ground objects such as field boundaries and crop rows. Thus, linear feature extraction(edge detection) is an important task for boundary delineation and crop row detection.

Over the years, many methods have been proposed to delineate field boundaries using semi-automatic and automatic methods (Ji, 1996), (Reyberg et al., 2001), (Torre & Radeva, 2000), (Turker & Kok, 2013). Standard edge detection methods work reasonably well in Western Europe and North America. But these methods fail to detect field boundaries in the study area Mali (STARS project, personal communication). The main problems are vague field boundaries and spatial heterogeneity of the regions on the both sides of the boundary.

Low and medium resolution satellite images have limited capacity to offer accurate information for field level. Moreover, they are not suitable for crop rows detection due to the small size of the elements to detect. On the other hand, very high resolution satellite images contain rich and detailed ground information, and they can reflect farm field information accurately to sub-meter level. But due to the complex ground environment, extracting the required information from very high resolution satellite images is a big challenge. Therefore, it is of importance to develop methodology that facilitates automatic extraction of linear features (edges) that represent field boundaries and crop rows from very high resolution satellite imagery.

1.2. Background

This part gives background knowledge on different edge detection techniques including line segment detector. It also gives a general idea about image segmentation and related concepts like texture.

Edge detection

An edge is a part of the image where the brightness of the image changes abruptly. Edge detection is a process of detecting and locating sharp discontinuities in the grey values of an image (Ziou & Tabbone, 1998). Many edge detection methods have been developed. The performance of an edge detection operator highly depends on lighting conditions and noise (Bhardwaj & Mittal, 2012). Most edge detection algorithms work well only in the images with sharp intensity transitions. They are also sensitive to noise. For this reason, smoothing operation is required to reduce noise in the image before the actual edge detection. This smoothing has a negative effect as it distorts the edge information. To keep balance between edge information and smoothing, the image is filtered with appropriate kernel such as Gaussian kernel. Due to the presence of noise the operators extract false edges. The operators also fail to find the boundaries of objects that have a small change in intensity values or change in intensity that occurs over a long distance, that leads to both problems of detection and localization of edges (Bhardwaj & Mittal, 2012). Therefore, problems of false edge detection, missing edges and poor localization of edges limit the applicability of the algorithms.

Recently, a number of edge detection methods based on Gestalt theory and Helmholtz principle were presented. Gestalt theory describes the laws of human visual reconstruction and Helmholtz principle states that noticeable structures may be viewed as exceptions to randomness (Tepper et al., 2014). Moisan and Morel (2000) applied edge detection methods, without any a priori information, based on the Gestalt theory and the Helmholtz principle. According to a basic principle of perception due to Helmholtz, an observed geometric structure is “meaningful” if it has a low probability to appear in a randomly created image (Desolneux et al., 2003). This is called “a contrario” approach. In this approach, instead of characterizing the elements we wish to detect, on the contrary, we characterize the elements we wish to avoid detecting. When an element sufficiently deviates from the background model, it is considered as meaningful and hence, detected (Tepper et al., 2014). To any geometric event on an image there is number of false alarms (NFA) associated to it. The NFA of an event is defined as the expectation of the number of occurrences of the event in a pure noise image of the same size.

Line Segment Detector

Line segments provide expressive information about the geometric content of images. Many algorithms have been developed and implemented to extract line segments from images. Hough Transform (HT) is one well known method to detect lines from images (Nixon & Aguado, 2012). Other recent implementation is a line segment detector (LSD) algorithm presented by Grompone von Gioi et al. (2012) built on the method of Burns et al. (1986). It integrates line segment detection with the Helmholtz principle. The LSD algorithm is currently developed to detect straight line segments from images. It is only suitable to detect straight edges from images. Nevertheless, large parts of the edges (for example field boundaries) are not really straight, but curved.

Image Segmentation

Image segmentation is a division of an image into multiple sub-regions based on a desired feature. There are two main approaches to segment images: edge-based and region-based (Faruquzzaman et al., 2008). Edge-based segmentation partitions the image into sub-regions by looking for discontinuities in image intensity, whereas region-based segmentation methods partition the images into different sub-regions of closed boundaries with the assumption that pixels in the same category have certain homogeneity in

spectral values (Evans et al., 2002). Region based segmentation may be classified as the bottom-up approach which merges smaller region into larger ones, top-down approach which splits an image into smaller regions and the mixed approach which leads to splitting and merging regions (Faruquzzaman et al., 2008). There are several measures that are used to decide whether regions should be merged or split. Texture measure is one of them.

Texture

Texture is an important spatial feature that is used for analysis and interpretation of digital images. According to Haralick (1979), texture is defined as the spatial variation in image intensities. It describes visual information that is related to local variation in orientation, color and intensity in an image (Min, 2015). Texture analysis requires the identification of important features that differentiate the textures in the image for classification, segmentation and recognition (Arivazhagan & Ganesan, 2003). The gray level co-occurrence matrix (GLCM), introduced by Haralick et al. (1973) as “gray-tone spatial-dependence matrix”, shows different combinations of gray levels occurrence in an image. A number of statistical texture features can be computed from GLCM. Statistics are classified as first order, second order or higher order statistics depending on the number of pixels in each combination. Homogeneity, dissimilarity, entropy, mean, standard deviation, contrast, energy and correlation are the most widely used second order statistics in the remote sensing imagery analysis. The construction of gray-level co-occurrence matrix depends on different parameters: the number of gray levels used in the matrix, the window size, the distance and the orientation. There are also other simple statistical texture measures that use edge density and direction to characterize the texture.

This research focuses on one specific topic on the larger STARS frame, that is, automated farm field delineation and crop row detection from satellite images. Conventional edge detection methods have been used for farm field boundary delineation. But, these methods are not efficient to detect field boundaries when fields have complex landscapes. The LSD algorithm is currently developed to detect straight line segments from images and is successful to automatically detect straight linear features from images. Therefore, modifying the LSD algorithm and using its capability for boundary delineation and crop row detection is an important task. The capabilities of very high resolution satellite imagery (both in spatial and spectral) with appropriate methodology gave opportunity to investigate the above mentioned problem and test in a test area in Mali.

1.3. Research Identification

1.3.1. Research Objective

The main objective of this research is to develop a procedure and implement image analysis methods to adapt the line segment detection algorithm and make it applicable for farm field boundary delineation and crop rows detection from very high resolution satellite imagery.

Research Sub- Objectives

1. To identify the influence of the internal parameters of the algorithm on the quality of the results.
2. To identify the appropriate band as an input for LSD algorithm.
3. To compare and select textural features characterizing farm fields from satellite images.
4. To accurately locate crop rows from satellite images.
5. To develop validation methods for evaluation of the result.

1.3.2. Research Questions

1. What are the optimal values of the parameters for the proposed applications?
2. How to incorporate multispectral information as an input to LSD algorithm?

3. Can texture help in the field boundary delineation? If so, which texture measure and distance in GLCM processing are appropriate?
4. What is the dominant orientation of crop rows in a particular field?
5. How successful is LSD in detecting field boundaries and crop rows?
6. Do accuracy measures positional accuracy, correctness, completeness, false detection ratio and missing detection ratio fit for a particular purpose?

1.4. Innovation aimed at

The novelty in this study is to adapt the line segment detector (LSD) algorithm and make it applicable for automated agricultural farm field boundary delineation and crop row detection from satellite images.

1.5. Method adopted

The flow chart in Figure 1.1 shows an overview of the methodology followed to reach the objectives and answer research questions. The detail process is further explained in Chapter 4.

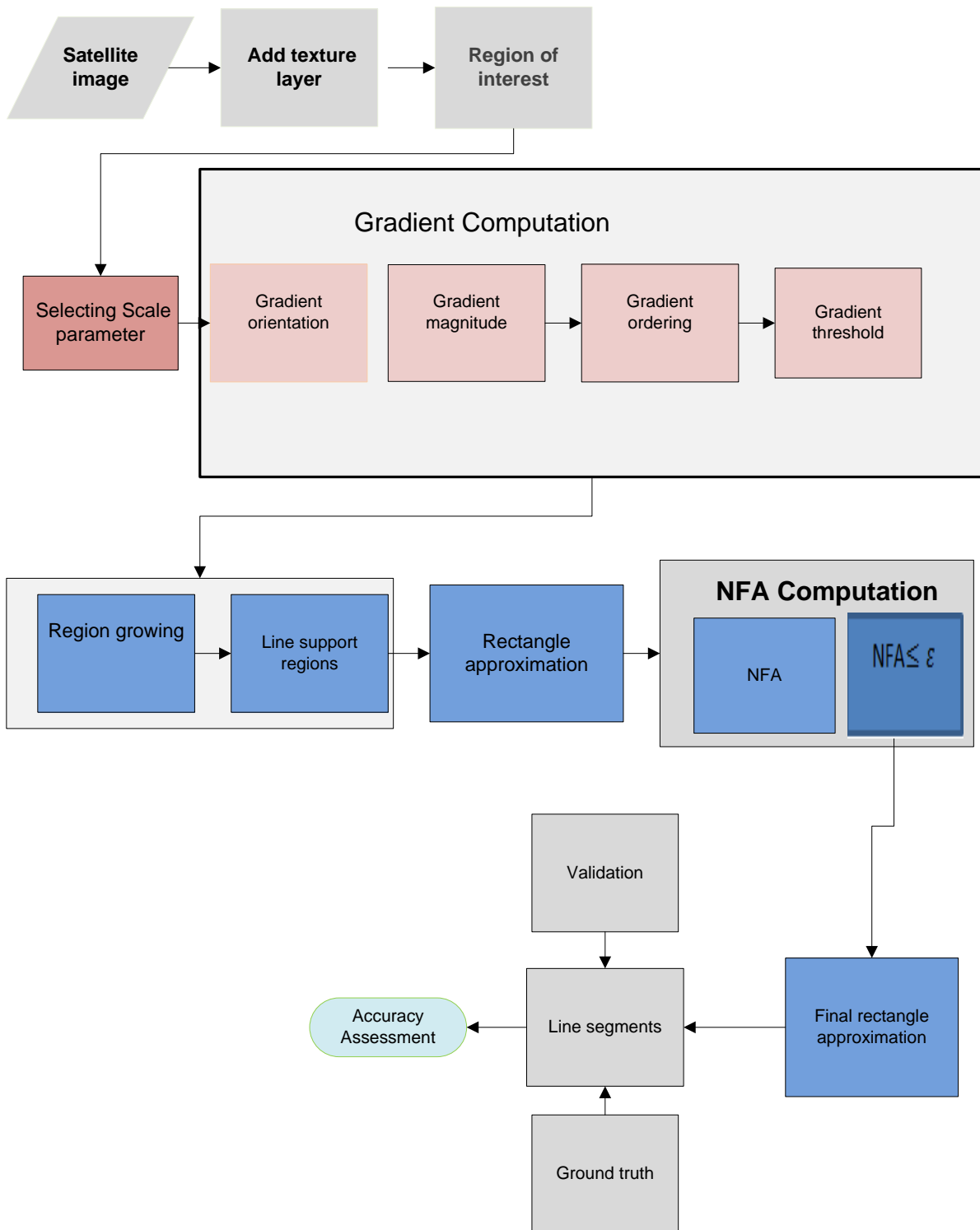


Figure 1.1: Flowchart of the methodology

1.6. Outline of the thesis

Chapter 2 is a literature review on Boundary concepts, Gestalt theory and The Helmholtz Principle and texture information for image segmentation.

Chapter 3 describes the study area and the data used in this research.

Chapter 4 presents the methodology applied in this research.

Chapter 5 discusses the results of the study.

Chapter 6 describes general discussions.

Chapter 7 gives summary of conclusions and recommendation.

2. LITERATURE REVIEW

2.1. Boundary concepts

Dale &McLaughlin (1988) define boundary in legal sense as “a vertical surface that defines where one land owner’s territory ends and the next begins.” Williamson et al. (2010) provided a comprehensive definition of the term boundary as “either the physical objects that mark the limits of a parcel, property, or interest in land or an imaginary line or surface making or defining the division between two legal interests in land.” According to Oxford Dictionary, the words ‘field’ and ‘boundary’ are defined as: Field, “an area of open land, especially one planted with crops or pasture, typically bounded by hedges or fences”. Boundary, “line which marks the limits of an area; a dividing line.” A more specific definition of boundary is the one given by Jing et al. (2011), boundary as an imaginary line that marks the bounds of two adjoining parcels of land. There are two broad categories of boundaries: fixed boundaries and general boundaries (Dale &McLaughlin, 1988). Fixed boundaries are boundaries that can be surveyed accurately and expressed by bearings and distances, or by coordinates whereas general boundaries are boundaries where the precise line of boundary between adjacent parcels has not been determined, but, it is usually represented by either natural or man-made physical features like fences, hedges, roads etc. (Williamson et al., 2010). Different rules of interpretation and definition of boundaries apply depending on the nature and type of boundaries. Therefore, in this research field would be related to land use and crop type, whereas boundaries would be related to edge features where changes in these types take place. A similar conclusion is also drawn by Yan and Roy (2014) and Ji (1996).

2.2. Gestalt theory and The Helmholtz principle

Gestalt theory is a branch of psychology which focuses on human visual perception of objects and tries to explain how human mind perceives and recognizes patterns (Chang et al., 2007), (Sarkar & Boyer, 1993). According to this theory, whenever points have common properties, they get grouped and form a new bigger visual object, a “Gestalt.” (Desolneux et al., 2003). Gestalt theory emphasizes holistic nature of objects rather than parts during human visual perception (Jiang et al., 2006). A set of Gestalt rules were formulated to describe the grouping mechanisms of how fundamental geometric elements are perceived as a whole, rather than an individual collection of parts by humans. Grouping characteristics can be any property of the points, such as proximity, colour, alignment, parallelism, common orientation or closure. The Helmholtz principle is a perception principle which introduces a method for computing geometric structure in a digital image by controlling both false negative and false positive (Grompone von Gioi et al., 2008). If a particular configuration of points sharing common characteristics is observed in an image, the Helmholtz principle examines whether this common feature is occurring by chance or not by using an “a contrario” assumption. Following this assumption, if p is the probability that an object has a certain property, then the probability that at least k objects out of the observed n have this property is given by the tail of the binomial distribution, i.e.

$$B(n, k, p) = \sum_{i=k}^n \binom{n}{i} \cdot p^i \cdot (1 - p)^{n-i} \quad (2.1)$$

If N is the number of different point configurations of the event, then the Number of False Alarms (NFA) of the event is

$$NFA = N \cdot B(n, k, p) \quad (2.2)$$

Meaningful events will then be events with a very low NFA. The event is called ε -meaningful if $NFA < \varepsilon$ under the uniform random assumption (Desolneux et al., 2003). This concept can be applied for linear segments. If l is a segment with length n that contains at least k points that have the same orientation as l in an image of size $N \times N$, then the Number of False Alarms (NFA) associated with the segment is

$$NFA = N^4 \sum_{i=k}^n \binom{n}{i} \cdot p^i \cdot (1-p)^{n-i} \quad (2.3)$$

where N^4 is an approximate number of potential segments in $N \times N$ image (Desolneux et al., 2003).

2.3. Texture information for image segmentation and boundary mapping

Texture measures have been used widely in remote sensing, particularly with high and very high resolution images and with panchromatic imagery (Epifanio & Soille, 2007). Texture features can be vital for image segmentation and can be used as the basis for classifying image parts (Davis et al., 1979). Several studies have shown that classification of high spatial resolution images can be improved by the use of texture (Ryherd & Woodcock, 1996), (Franklin et al., 2000). When land covers exhibit similar spectral characteristics and make classification difficult, the use of texture information is a potential solution (Lloyd et al., 2004). Incorporating texture measures could enhance the discrimination between spectrally similar classes (Blaschke, 2010).

2.4. Related works

There are some considerable results achieved by previous researchers on the development of semi-automatic and automatic field boundary delineation and crop rows detection.

Janssen and Molenaar (1995) developed a three-stage strategy for updating both the agricultural field boundaries and the crop type of the agricultural fields using a Landsat Thematic Mapper image. In the first stage, fixed geometric data already stored in the GIS is integrated with the output of the edge detection procedure applied to Landsat Thematic Mapper image. In the second stage, object based classification is used to determine crop type of fields. In the third stage, post processing (merging) is applied to solve problem of oversegmentation. The authors reported that there was 87% agreement between the resulting field geometry and the field geometry by the photo-interpreter.

Ji (1996) tried to extract field boundaries from a single date Landsat Thematic Mapper imagery by adopting a dyadic wavelet transform method. It was reported that the majority of field boundaries were delineated by the adopted methodology. However, the use of a single date image failed to delineate boundaries between two fields when the fields have similar spectral properties. Manual editing was required to delineate the remaining boundaries. The use of multi-temporal data set with a fully automated algorithm were recommended to obtain a complete delineation.

Torre & Radeva (2000) used a semi-automatic method to segment agricultural fields. They combined region growing and deformable models (snakes). They considered different aspects like parameterization, user interaction and convergence criteria to assure optimal image segmentation. The role of the operator was to give seed region to initialize the snake. The algorithm was tested for over 20 different aerial images, having 30 parcels per image on the average, and detected 70 % of the cases successfully.

Rydberg et al. (2001) presented a multispectral segmentation method for detecting agricultural field boundaries from remote sensing images. The method was applied in the southern part of Sweden using multispectral SPOT and Landsat TM images. The method was developed to integrate the segmentation algorithm with the edge information from gradient edge detector, where the information from all selected image bands is utilized in both procedures. In this way, information from several bands and from different dates can be used to delineate field boundaries with different characteristics. This is especially vital for agricultural applications, when multi-date information is required to differentiate crops, trees, shrubs and other objects like roads. The method identified 87% of the edges correctly as compared to the edges of the ground truth.

Evans et al. (2002) proposed a method, called canonically- guided region growing (CGRG), for the automated segmentation of the agricultural area in Western Australia into field units from multispectral Landsat TM images. The procedure has the assumption that each field has only a single ground cover and that the width of the minimum field of interest is known. The method worked well for the majority of the sample images.

Butenuth et al. (2004) described an automatic method to extract boundaries of fields from aerial images. First, watershed segmentation was carried out to segment field areas based on the gradients in the course scale of the imagery. Next, GIS knowledge on fixed field boundaries was introduced to support the segmentation. This provides a topologically correct framework of the field boundaries. Finally, snakes were used to improve the geometrical correctness by taking the topological constraints into consideration. The results showed the potential of the proposed method.

Mueller et al. (2004) presented an object-oriented approach for the extraction of large, human-made objects, especially agricultural fields, from high resolution panchromatic satellite imagery focussing on shape analysis. Four different images from different sensors having different resolutions were used to test the proposed approach. Comparisons of the presented approach with standard methods revealed the advantages of the presented method.

In the work of Ishida et al. (2004), a multi-resolution wavelet transform method was applied to detect the edges of submerged paddy fields. The method was applied on SPOT image to prepare a base map that defines sections (parcels) of fields. The results obtained were reported to be satisfactory in practice and the methodology could be applied to other paddy fields.

Da Costa et al. (2007) proposed an algorithm to automate the delineation of vine parcels from WorldView-2 images using an object-based classification model. They applied the method in the Bordeaux, wine producing area, in France. The approach uses texture attributes of vine parcels to identify vine and non-vine pixels and gives encouraging results. However, errors in the segmentation occasionally occur at the beginning of the season or in areas with young plants.

In the work of Tiwari et al. (2009), semi-automatic extraction of field boundaries from high resolution satellite data was presented. The methodology was applied to a certain agricultural area in India using an IRS P-6 LISS IV dataset. Tonal and textural gradients were used to segment the regions and these regions were classified to derive preliminary field boundaries. Finally, snakes were used to refine the geometry of the preliminary field boundaries. Most of the extracted boundaries coincide with the reference which shows the potential of the proposed solution.

Sainz-Costa et al. (2011) presented a strategy for identifying crop rows by analyzing video sequences acquired from a camera mounted on top of an agricultural vehicle. They applied gray scale transformation (convert an RGB image into black and white image), and then the image is changed to a binary image by thresholding. To identify crops and rows, rectangular patches are drawn over the transformed binary image. The gravity centers of the patches are used as the points defining the crop rows and a line is adjusted by considering these points.

Ali (2012) introduced the use of Very High Resolution satellite panchromatic/colour imageries and handheld GPS navigation receiver to develop a method for cadastral surveying by using on screen digitization techniques. The study showed that by using his newly developed technique more parcels can be surveyed in a shorter period of time as compared to the traditional cadastral parcel boundaries surveying method.

Ursani et al. (2012) proposed a new procedure for agricultural land use mapping from a pair of very high resolution multispectral and panchromatic satellite images. Spectral and texture information were used to classify the images. Unsupervised classification was used to split a multispectral image into spectrally homogeneous non-contiguous segments. In parallel, texture-driven supervised classification was used to split the panchromatic image into a grid of square blocks. Finally, a land use map was generated by fusing both spectral and textural classification results. It was reported that both qualitative and quantitative evaluations of the results showed good results. Moreover, fusing the spectral and textural classification results improves the accuracy as compared to individual classification results.

Turker and Kok (2013) used perceptual grouping of Gestalt theory for automatic extraction of dynamic sub-boundaries within agricultural fields of remote sensing imagery. The methodology was applied in the Marmara region of Turkey using SPOT4 XS and SPOT5 XS images. Field boundary data and satellite imagery were integrated to perform field-based analysis. Canny edge detector was used to detect the edge pixels. The overall matching percentages between the automatically extracted and the reference data were 82.6% and 76.2% for SPOT5 and SPOT4 images respectively.

Recently, Sidiropoulou Velidou et al. (2015) presented a Gestalt-based line segment method to detect geological lineaments automatically from remote sensing imagery. The study area was selected in Kenya and an ASTER image was used to apply the methodology. To assess the accuracy, false detection rate and missing detection rate were calculated and the values were both equal to 0.5. The method worked well to extract geological lineaments from remote sensing imagery. The algorithm could be extended to detect other features from remotely sensed data.

2.5. Accuracy Assessment

The automatically extracted farm field boundaries can be compared with the manually digitized boundaries of the reference data by adopting accuracy assessment methods proposed in literature. Heipke et al. (1997) proposed several quality measures to perform accuracy assessment of road extraction. Correctness and completeness are the most widely used. These quality measures can also be applied to assess the quality of automatically extracted buildings (Rutzinger et al., 2009) or line segments (Lin et al., 2015). The correctness represents the part of the extraction which matches the reference within a buffer around the reference. The completeness, also referred to as Detection Rate, is defined as the part of the reference that matches the extraction within a specific buffer around the extracted result. Another novel accuracy assessment method is the one developed by Sidiropoulou Velidou et al. (2015) to assess the accuracy of automatically detected geological lineaments. False detection rate and missing detection rate were used to assess the quality.

3. DATA

This chapter explains the study area, the imagery and software used in this research. Section 3.1 provides details of the study area, section 3.2 describes the data characteristics and section 3.3 gives the list of software used. $5^{\circ}13'53.18''\text{W}, 12^{\circ}13'1.83''\text{N}$.

3.1. Study area

The study area for this research is located in the southern part of Mali, in Western Africa (Figure 3.1). Its location is $5^{\circ}13'53.18''\text{W}, 12^{\circ}13'1.83''\text{N}$. It covers an area of approximately 67 square kilometers. The landscape in Mali is heterogeneous and is characterized by variable plant growth, small field sizes with trees inside in almost all fields, mixed cropping systems and variable cropping dates. Farming is the main source of income for most people of the region. The main crop types in the area are cotton, maize, millet, peanuts and sorghum. Most of the crops are sown between May and July and harvested from September to November. Precipitation in the area is around 800 mm per year.

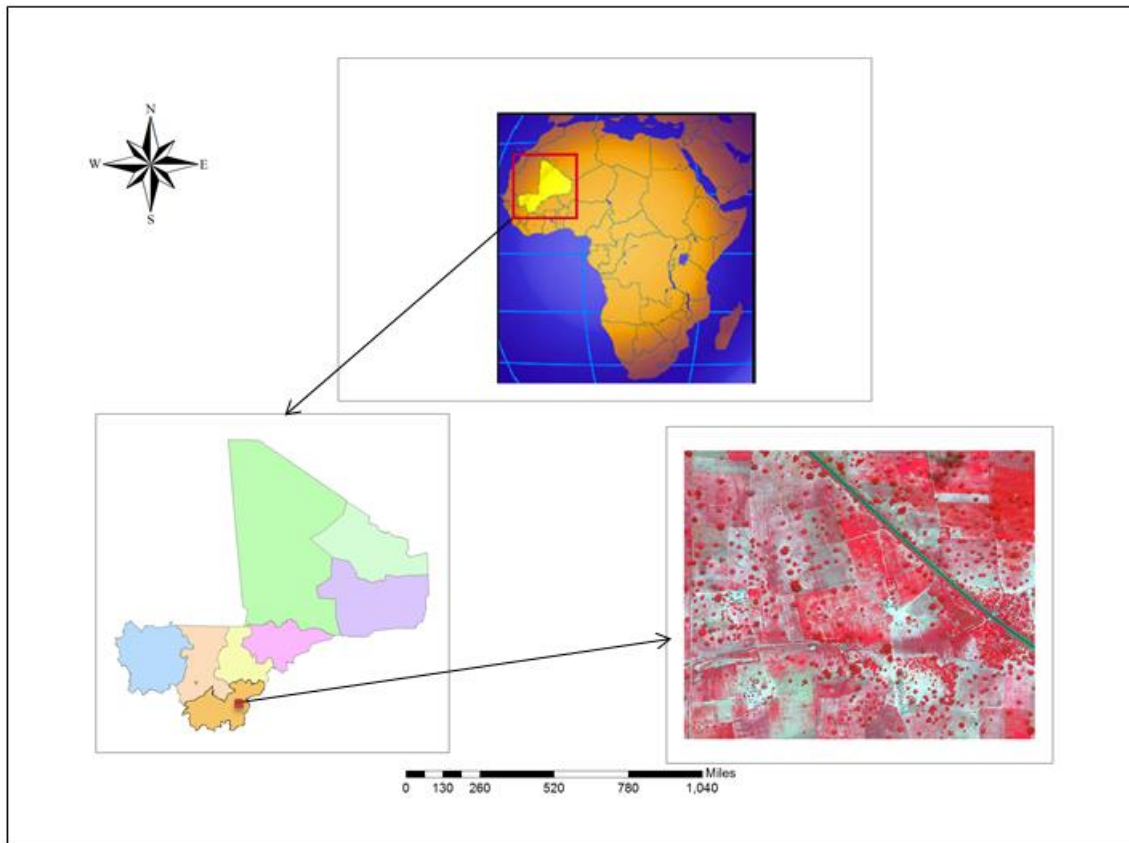


Figure 3.1: Study area

3.2. Imagery and Reference data

3.2.1. Very High Resolution Satellite image

The imagery used for this research is Very High Resolution satellite image of WorldView-2 acquired on July 29, 2014. The spatial resolution for the panchromatic band is 0.46m with spectral range from 450 to 800nm. The multispectral image has a spatial resolution of 2m and the image is composed of eight bands: Coastal Blue (400 to 450nm), Blue (450 to 510nm), Green (510 to 580nm), Yellow (585 to 625nm), Red (630 to 690nm), Red Edge (705 to 745nm), Near Infrared-1 (770 to 895 mm), and Near Infrared-2 (860 to 900nm). The specification of each band is given in Table 3.1.

Table 3.1: WorldView-2 satellite image specifications.

	GSD Pan (m)	GSD MS (m)	Swath nadir (Km)	Spectral Range Pan	Spectral Range MS
WorldView2	0.46	2.0	16.4	450-800nm	400-450nm(coastal) 450-510nm(blue) 510-580nm(green) 585-625nm(yellow) 630-690nm(red) 705-745nm(red edge) 770-895nm(near IR-1) 860-900nm(near IR-2)

3.2.2. Reference data

The reference datasets used for this research are

- A manually delineated field boundary of the study area from WorldView-2 multispectral image acquired on July 29, 2014 and
- Manually delineated crop rows from panchromatic image acquired on September 12, 2015. Different subsets are presented in the Appendix.

3.3. Software

In this research, the following software were used.

- ArcGIS version 10.3.1 was used for on screen digitization of reference data.
- ENVI, which was used for texture GLCM computation
- ERDAS Imagine 2015 which was used for subset selection and processing the data.
- R version 3.3.2 which was used for statistical computing, graphics and data analysis.

Moreover, the following R packages were used.

- rgdal
- raster
- mmand
- Rcpp
- inline
- sp
- stats
- circular

4. METHODOLOGY

This chapter describes the methodology followed to achieve the research objectives and answer research questions.

4.1. Texture calculation

The GLCM is one of the most popular methods to compute how often different pairs of grey levels of pixels occur in an image. The size of a GLCM is determined by the maximum grey value of the pixel. Pixel relationships in GLCM can be defined by varying distances and orientation. Since each pixel has eight neighboring pixels, there are eight choices for the orientation. However, taking the definition of GLCM into account, the possible ways of angle orientations are reduced to four, namely 0° , 45° , 90° and 135° as shown in Figure 4.1. Example of formation of GLCM for distance $d = 1$ in the horizontal direction (0°) is shown in Figure 4.2. The occurrence of pixel intensity 0 with pixel intensity 1 as its neighbor at a distance $d = 1$ in the horizontal direction is 3. Thus, the GLCM matrix row 0, column 1 is given a value of 3. Similarly, GLCM matrix row 2 column 2 is also given a value of 5, because there are five occurrences of pixel intensity 2 as pixel intensity 2 as its neighbor (for $d = 1$ in the horizontal direction). As a result, the input image matrix (Figure 4.2a) can be transformed into GLCM (Figure 4.2b).

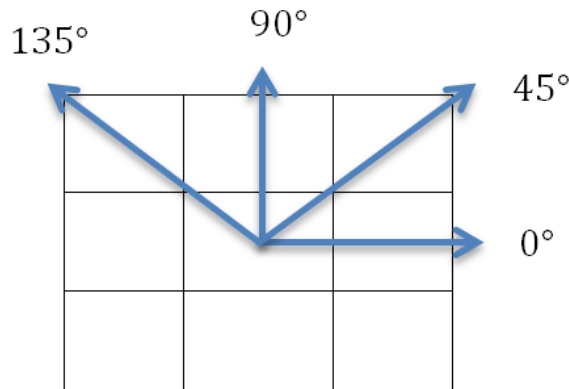


Figure 4.1: The four directions for calculating texture features.

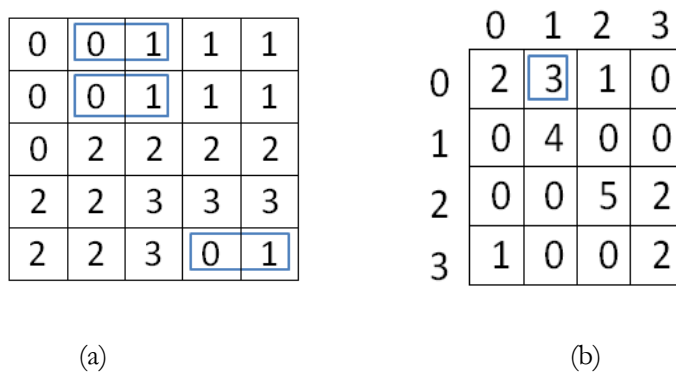


Figure 4.2: (a) Example of input image with 4 grey levels (b) GLC M for distance $d = 1$ and direction 0° .

Several texture measures can be computed from GLCM that provide texture information of an image. The eight second order statistics are listed below, where $P_{i,j}$ is the normalized grey level in the cell $(i,j)^{th}$ of the matrix, N is the number of rows or columns (Haralick et al. 1973).

4.1.1. GLCM contrast

GLCM contrast measures the amount of local variation of grey levels in the grey-level co-occurrence matrix. GLCM contrast can be computed as follows:

$$Contrast = \sum_{i,j=0}^{N-1} P_{i,j} (i - j)^2 \quad (4.1)$$

4.1.2. GLCM dissimilarity

$$Dissimilarity = \sum_{i,j=0}^{N-1} P_{i,j} |i - j| \quad (4.2)$$

4.1.3. GLCM homogeneity

Homogeneity measures the closeness of the distribution of the grey level co-occurrence matrix. It ranges on the interval $[0, 1]$ and is computed as follows:

$$Homogeneity = \sum_{i,j=0}^{N-1} \frac{P_{i,j}}{1+(i-j)^2} \quad (4.3)$$

4.1.4. GLCM entropy

GLCM entropy can be calculated as follows:

$$Entropy = \sum_{i,j=0}^{N-1} P_{i,j} (-\ln P_{i,j}) \quad (4.4)$$

4.1.5. GLCM angular second moment (ASM) and energy

GLCM angular second moment measures the local uniformity. Energy is the square root ASM

$$Angular\ second\ moment = \sum_{i,j=0}^{N-1} P_{i,j}^2 \quad (4.5)$$

4.1.6. GLCM mean

The GLCM mean is computed as follows:

$$\mu_i = \sum_{j=0}^{N-1} i(P_{i,j}) , \mu_j = \sum_{i=0}^{N-1} j(P_{i,j}) \quad (4.6)$$

4.1.7. GLCM variance

$$\sigma_i^2 = \sum_{j=0}^{N-1} P_{i,j} (i - \mu_i)^2 , \sigma_j^2 = \sum_{i=0}^{N-1} P_{i,j} (j - \mu_j)^2 \quad (4.7)$$

4.1.8. GLCM correlation

GLCM correlation measures the spatial linear dependency of the grey levels. It can be computed as follows:

$$Correlation = \sum_{i,j=0}^{N-1} P_{i,j} \frac{(i-\mu_i)((j-\mu_j))}{\sigma_i \sigma_j} \quad (4.8)$$

In this research, the effects of all the eight second order GLCM texture measures on detection of farm field boundary were examined. As neighboring pixels are more likely to be correlated than pixels far apart, three distance values $d = 1, 2, 3$ pixels in all four different orientations ($0^\circ, 45^\circ, 90^\circ$ and 135°) were tested.

4.2. Line Segment Detection Algorithm

The LSD algorithm, a technique developed based on the method of Burns et al. (1986), integrates line segment detection with the Helmholtz principle. The algorithm starts by calculating the level-line angle for each pixel based on pixel gradient. Level-line angles are angles that show the direction of the dark to light transition (edge) and these angles are used to form line-support regions (group of neighboring pixels with similar level-line angles). Each line-support region is a potential candidate for a segment and is validated based on the calculation of a Number of False Alarms (NFA) of the corresponding geometrical event associated with it. If the NFA is very low, then the segment is meaningful and thus, considered as a true detection. The complete Pseudo code of the LSD algorithm is given below.

Algorithm 1: LSD line segment detector

input: An image I

output: A list out of rectangles

```

1   $I_s \leftarrow \text{ScaleImage}(I, \text{scale}, \sigma)$ 
2   $(\theta, |\nabla I_s|, \text{OrderedListPixels}) \leftarrow \text{Gradient}(I_s)$ 
3   $\text{Status} \leftarrow \begin{cases} \text{Unavailable}, & \text{pixels with } |\nabla I_s| \leq \rho \\ \text{Available}, & \text{otherwise} \end{cases}$ 
4  foreach pixel  $P \in \text{OrderedListPixels}$  do
5      if  $\text{Status}(P) = \text{Available}$  then
6           $\text{region} \leftarrow \text{RegionGrow}(P, \tau)$ 
7           $\text{rect} \leftarrow \text{Rectangle}(\text{region})$ 
8          while  $\text{AlignedPixelDensity}(\text{rect}, \tau) < D$  do
9               $\text{region} \leftarrow \text{CutRegion}(\text{region})$ 
10              $\text{rect} \leftarrow \text{Rectangle}(\text{region})$ 
11         end
12          $\text{rect} \leftarrow \text{ImproveRectangle}(\text{rect})$ 
13          $\text{nfa} \leftarrow \text{NFA}(\text{rect}, \tau)$ 
14         if  $\text{nfa} \leq \varepsilon$  then
15             Add  $\text{rect}$  to out
16         end
17     end
18 end

```

The LSD algorithm has three parameters: scale s , angle tolerance τ and detection threshold ε .

Scale parameter

The scale parameter is one of the main parameters of the LSD algorithm. It helps to get a better representation by emphasizing certain features and facilitates automatic detection of the required features.

LSD results are different when the algorithm is applied at different scales (Grompone von Gioi et al., 2012). Some objects in an image only may exist as meaningful entities over a certain range of scales (Desolneux et al., 2003). Thus, the scale parameter used in the LSD algorithm makes a clear relation between structures at different scales.

Angle tolerance

The angle tolerance τ in the LSD algorithm is used to combine pixels into line-support regions. It is calculated from $180^\circ/d$, where the parameter d is the number of different orientations. This implies that for $d = 16, 8, 4$ the angle tolerance $\tau = 11.25^\circ, 22.5^\circ$ and 45° respectively. The default value of d is 8.

Detection threshold

The detection threshold parameter explains the confidence limit for the region. It is related to the NFA value and is given by $\varepsilon = -\log(\max.NFA)$. The NFA is used to decide whether the event is meaningful or not. The smaller the NFA, the more meaningful the detected event is (Desolneux et al., 2008).

4.2.1. Multispectral analysis

The image used in this research is a multispectral WorldView-2 image. The LSD algorithm takes only a single band as an input to detect line segments. However, information from all bands might be required to increase the capability of the LSD. Comparison of multi spectral information against single band information was performed. In order to concentrate all the available information, the gradient information in eight bands has to be combined as a single band to be as an input for LSD algorithm. This was done by taking the vector sum of gradients of all eight bands.

4.2.2. Image scaling

The first step of LSD is image downscaling of the input image. This is performed to cope with some quantization problems and aliasing. A Gaussian filter is applied to keep balance between avoiding aliasing and avoiding image blurring (Grompone von Gioi et al., 2012). The standard deviation of the Gaussian kernel is given $\sigma = \frac{0.8}{S}$.

4.2.3. Gradient computation

The image gradient reveals a directional change of image intensity between neighboring pixels in an image. The gradient magnitude tells us how fast the image is changing, while the gradient direction tells us the direction in which the image changes most rapidly. The gradient computation at pixel (x, y) is performed using a 2×2 mask (Figure 4.3). This mask was chosen to minimize the dependence of the computed gradient values so that pixel independence is preserved as much as possible (Moisan and Morel, 2000).

...	⋮	⋮	...
...	$I(x, y)$	$I(x+1, y)$...
...	$I(x, y+1)$	$I(x+1, y+1)$...
...	⋮	⋮	...

Figure 4.3: Gradient computation using 2×2 mask.

Let $I(x, y)$ denote the gray level value at pixel (x, y) . The image gradient at (x, y) is calculated

$$g_x(x, y) = \frac{I(x+1, y) + I(x+1, y+1) - I(x, y) - I(x, y+1)}{2} \quad (4.9)$$

$$g_y(x, y) = \frac{I(x, y+1) + I(x+1, y+1) - I(x, y) - I(x+1, y)}{2} \quad (4.10)$$

The gradient magnitude is computed as

$$g(x, y) = \sqrt{g_x^2(x, y) + g_y^2(x, y)} \quad (4.11)$$

and the gradient orientation as

$$\varphi(x, y) = \arctan\left(\frac{g_y}{g_x}\right) \quad (4.12)$$

The level-line angle is orthogonal to the gradient orientation and shows the direction of the edge (Figure 4.5). Figure 4.4 shows the image gradient in the horizontal and vertical directions.

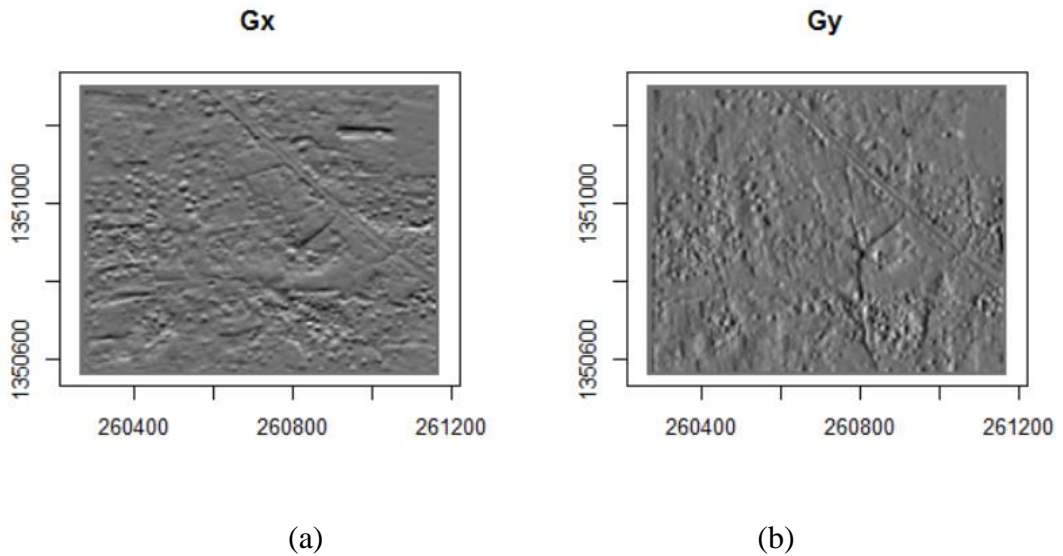


Figure 4.4: Image gradient. (a) Horizontal direction, (b) Vertical direction

In this research, to make use of all the available information present in all eight bands, the changes in x and y direction in each band are calculated and then combined as a vector sum

$$G_x(x, y) = \sum_{k=1}^8 g_x[k] \quad (4.13)$$

and

$$G_y(x, y) = \sum_{k=1}^8 g_y[k] \quad (4.14)$$

where $g_x[k]$ and $g_y[k]$ denote the changes in x and y directions of band k respectively. The gradient magnitude of the vectors sum is computed as

$$G(x, y) = \sqrt{G_x^2(x, y) + G_y^2(x, y)} \quad (4.15)$$

and gradient orientation is computed as

$$\theta(x, y) = \arctan\left(\frac{G_y}{G_x}\right) \quad (4.16)$$

The gradient magnitude and orientation computed using Equations (4.15) and (4.16) are used for the next steps of the LSD algorithm.

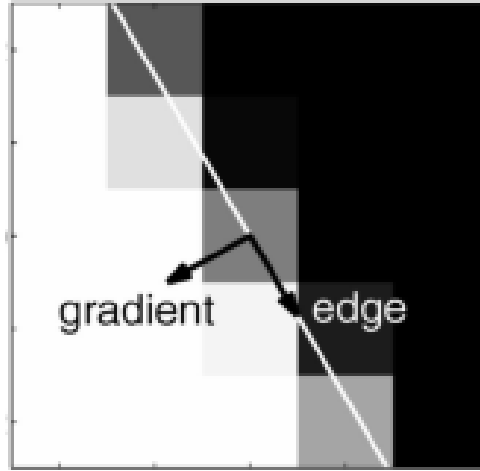


Figure 4.5: Edge orientation, reprinted from Meer and Georgescu (2001)

4.2.4. Gradient ordering and threshold

After calculating gradient magnitude and gradient orientation at each pixel, pixels are arranged in a decreasing order based on their gradient magnitude. Pixels with high gradient magnitude are expected to be edge pixels. So, it is reasonable to start at pixels with high gradient magnitude for region growing. But pixels with low gradient magnitude correspond to flat zones or smooth transitions. Thus, pixels with gradient magnitude less than a certain threshold value ρ are rejected and not considered in the construction of line-support regions. The threshold is set by the formula

$$\rho = \frac{q}{\sin\tau} \quad (4.17)$$

where the parameter τ is the angle tolerance to be used in the region growing algorithm and the parameter q is a bound on the possible error in the value of the gradient due to quantization noise and is set equal to 2 (Grompone von Gioi et al., 2012).

4.2.5. Region Growing

Having the magnitude and orientation of the image gradient, the next step is the formation of line-support regions. Pixels that share the same gradient orientation are grouped to form the line-support regions. The region growing algorithm starts from the first seed pixel from the ordered list and continues

to the second and so on to form a line-support region (Figure 4.6). The available neighboring pixels are tested recursively and the ones whose level-line angles are equal to the angle of the region up to a certain tolerance τ are added to the region. An 8-connected neighborhood is used. The initial region angle θ_{region} is set to the level-line angle of the seed pixel. Whenever a new pixel is added to the region, the region angle is updated by

$$\theta_{region} = \arctan\left(\frac{\sum_j \sin\theta_j}{\sum_j \cos\theta_j}\right) \quad (4.18)$$

where θ_j is the level-line angle of the newly added pixel and j runs over the region pixels. The process continues until no other pixel can join to the region.

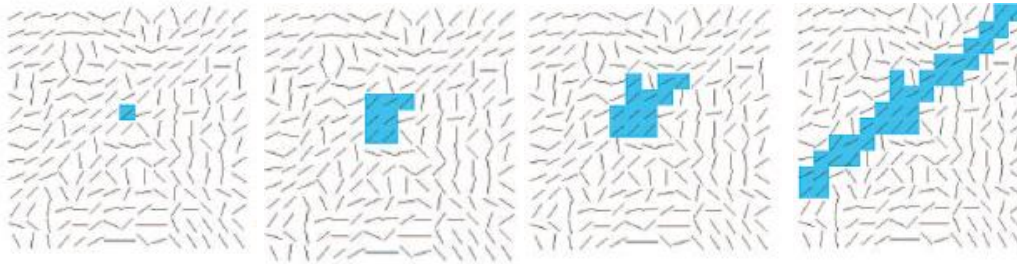


Figure 4.6: Regional growing process of aligned points, reprinted from Morel et al. (2010)

4.2.6. Line segment localization

Following the formation of a line-support region, the next step is determination of the location and orientation of the line segment (Figure 4.8). To do that, Burns et al. (1986) described a method to extract a straight line from the corresponding line-support region. In Burns' method, orientations of lines are estimated by fitting planes to pixel intensities over line-support regions. The locations of lines are obtained from the intersections of the horizontal plane and the fitted planes. The method provides accurate results, but it is computationally expensive (Yuan & Ridge, 2014). In this research, orientation of line is obtained by adopting Harris edge and corner detector method (Harris & Stephens, 1988). Let W be the line-support region. If pixel difference is taken by shifting the region W , the largest change occurs when the shift is orthogonal to the edge in the region, but the smallest change occurs when it is along the edge, that corresponds the line orientation. The shift vector resulting in the smallest change (that shows the line orientation) is the eigenvector corresponding to the smaller eigenvalue of the matrix

$$A = \begin{pmatrix} \sum_W I_x^2 & \sum_W I_x I_y \\ \sum_W I_x I_y & \sum_W I_y^2 \end{pmatrix} \quad (4.19)$$

where I_x and I_y are the derivatives in horizontal and vertical directions in the line-support region W .

To locate the line segment that is best aligned with the edge in the line-support region, Hough transform is used. The overall gradient magnitude that a line passes is examined and the one that gives the maximum value is selected. The Hough transform parameterizes a straight line using two parameters: ρ and θ by the equation

$$\rho = x \cos\theta + y \sin\theta \quad (4.20)$$

where ρ denotes the distance from the origin to the closest point of the straight line, and θ is the angle between the horizontal axis and the line that connects the origin with the closest point (Figure 4.7). All points that lie along a straight line in the Cartesian space can be represented by a point (ρ, θ) in the Hough space. Each point (ρ, θ) in the Hough space can be transformed to a straight line in the Cartesian space by the inverse Hough transform.

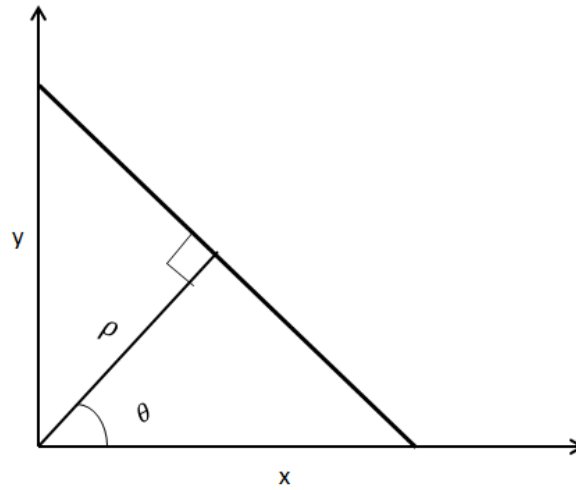
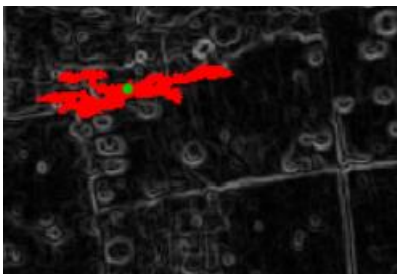
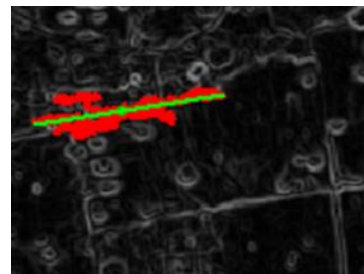


Figure 4.7: Representation of a line by ρ and θ .

Once we found the value of θ from the orientation of the line, each pixel location (x, y) in the line-support region is substituted into equation (4.20) weighted by its gradient magnitude to obtain a value of ρ . The maximum value of ρ together with θ define a unique line. And finally the line is drawn in the image plane.



(a) Line-support region.



(b) Line segment extracted from line-support region.

Figure 4.8: Example of a line-support region and its associated line segment.

4.2.7. Rectangular approximation

To validate whether a line-support region is meaningful or not, the geometrical event associated to it must be found. Here rectangles are used to approximate line-support regions. The gradient magnitude of each pixel is used as the pixel's "mass". And then, the center of mass of the region is used to select the center of the rectangle and the first inertia axis of the region to select the direction of the rectangle. The center of the rectangle (c_x, c_y) is computed as follows:

$$c_x = \frac{\sum_{j \in \text{region}} G(j) \cdot x(j)}{\sum_{j \in \text{region}} G(j)} \quad (4.21)$$

$$c_y = \frac{\sum_{j \in \text{region}} G(j) \cdot y(j)}{\sum_{j \in \text{region}} G(j)} \quad (4.22)$$

where, $G(j)$ is the gradient magnitude of pixel j in the region and j runs over all the pixels in the region. The direction of the rectangle is set to the eigenvector angle associated to the smallest eigenvalue of the matrix

$$M = \begin{pmatrix} m_{xx} & m_{xy} \\ m_{xy} & m_{yy} \end{pmatrix}$$

where

$$m_{xx} = \frac{\sum_{j \in \text{region}} G(j) \cdot (x(j) - c_x)^2}{\sum_{j \in \text{region}} G(j)} \quad (4.23)$$

$$m_{yy} = \frac{\sum_{j \in \text{region}} G(j) \cdot (y(j) - c_y)^2}{\sum_{j \in \text{region}} G(j)} \quad (4.24)$$

$$m_{xy} = \frac{\sum_{j \in \text{region}} (x(j) - c_x)(y(j) - c_y)}{\sum_{j \in \text{region}} G(j)} \quad (4.25)$$

Then, the smallest values of length and width of the rectangle are chosen to cover the full line-support region (Figure 4.9).

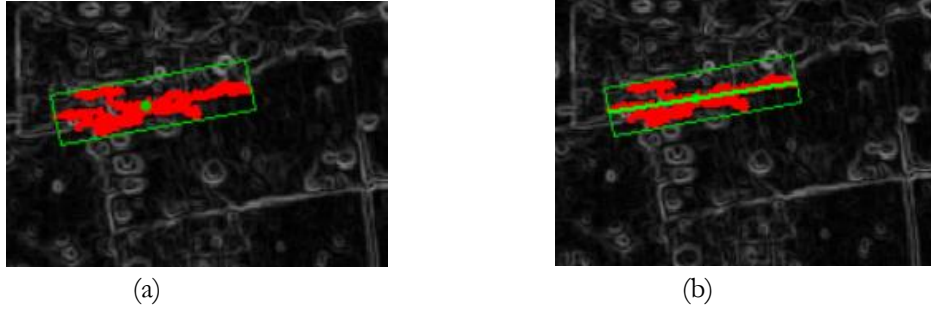


Figure 4.9: The smallest rectangle that covers all pixels of the line-support region: (a) without line segment. (b) with line segment

4.2.8. Number of False Alarms (NFA) computation

The Number of False Alarms (NFA) associated with the geometrical event (rectangle) is calculated based on the tail of the binomial distribution taking into account the dimensions of the image after scaling. The NFA associated with a rectangle r of the given image I with dimensions N and M is given by

$$NFA(r, I) = (NM)^{\frac{5}{2}} \cdot B(n, k, p) \quad (4.26)$$

where n, k are the total number of pixels and the total number of aligned points in the rectangle r respectively, and p is the probability that a randomly selected pixel in the rectangle is an aligned pixel (Grompone von Gioi et al., 2008). Finally, the ‘‘a contrario’’ model is used to validate whether it is a valid detection or not. Here, the background model is a gradient field where the gradient orientations of each pixel are independent and identically distributed (i.i.d) random variables. The rectangles with $NFA \leq \varepsilon$ are considered as meaningful. The lower the value of ε , the more meaningful the rectangle is.

4.3. Crop rows detection

Since most crops are sown and cultivated in rows, detecting crop rows automatically is an important task. Agricultural practices like planting, plant protection, weeding, spraying and harvesting require high precision and these tasks are repeated several times, which are very demanding for humans. Detecting crop rows automatically facilitate the automation of many of the agricultural activities which intern increase efficiency and improve yield. In addition to the location of crop rows, knowing accurate information on their orientation (the direction in which the plots are done) and spacing between them greatly assist in the monitoring of crops. The developed algorithm reports the line that represents the crop row, with the orientation of the line. From the orientation of the detected line segments, dominant orientation of rows is calculated. To make automatically detected line segments parallel to the x-axis and find the spacing between them (Figure 4.10), end points (x, y) of each line segment are rotated about the center of the image (c_x, c_y) using the formula

$$x' = (x - c_x)\cos\theta - (y - c_y)\sin\theta \quad (4.27)$$

$$y' = (x - c_x)\sin\theta + (y - c_y)\cos\theta \quad (4.28)$$

where θ is the negative of the dominant orientation of crop rows. The vertical distance between any consecutive parallel lines is the same as the distance between the points at which the lines intersect the y-axis. Since there may not be one to one correspondence between the number of automatically detected line segments and the number of crop rows in the reference dataset due to missing and false detections, the spacing between automatically detected line segments may not directly reflect the spacing between the actual crop rows. Nevertheless, the crop rows in the reference dataset almost have constant spacing (usually follow certain periodic nature). Therefore, it is of importance to find a technique that detects the hidden period from the spacing of the automatically detected line segments. Once we have found all the points of intersections of the y-axis and the automatically detected lines (after rotating the lines), the following procedures were followed to find the hidden period from the distribution of the points.

1. The Euclidean distance between every pair of points were calculated and a matrix with these distance values as entries was generated. That is, the matrix entries for pairs of points are the Euclidean distance between these pairs of points. These values are smaller when points are close and larger when points are far apart.
2. For different lag values, probability distributions of distance values that fall in the given interval were calculated. This was done by dividing the number of distance values that fall in the given interval to the total number of pairs of points.
3. The lag which yielded the highest probability (dominant frequency) was selected as the period for the distribution.

Finally, the period (lag), that was selected in step 3, was considered as the average spacing between crop rows.

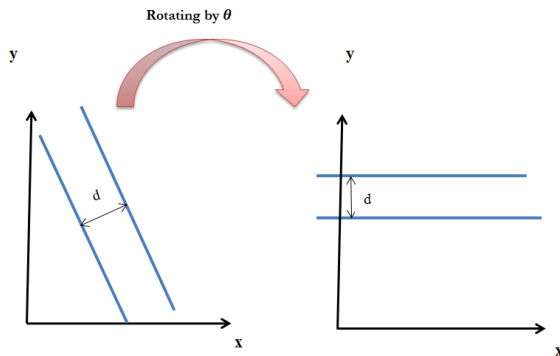


Figure 4.10: Rotating the lines by angle θ to make them parallel to the x-axis, d is the spacing between the lines.

4.4. Parameter tuning and validation

In this section, edge strength determination procedure and validation method for parameter tuning are presented. Contrast, width and steepness of line segments were used to determine the edge strength of segments. The validation method presented in this thesis assesses the correspondence between the reference and the detected datasets using two measures: ratio of missing detection (RM) and ratio of false detection (RF). To assess the positional accuracy of successful detections, mean and standard deviation of the distances of corresponding points were computed.

4.4.1. Edge Strength Determination

There are some basic attributes of a line that can be calculated from the line-support region, which reflect the strength of an edge. These include: length, width, contrast and steepness. These terms are defined as below (Burns et al., 1986).

- Length of the image line is the length of the segment of the line in its line-support region.
- Width of the image edge is the size of the interval, across the profile, within which the majority of the intensity change occurs. It is the width of its line-support region.

$$width = \frac{\text{area of the line support region}}{\text{length}} \quad (4.29)$$

- Contrast of the edge is the difference of the average intensities of the two sides of the line in the line-support region.
- Steepness of a straight edge is defined as

$$Steepness = \frac{\text{Contrast}}{\text{width}} \quad (4.30)$$

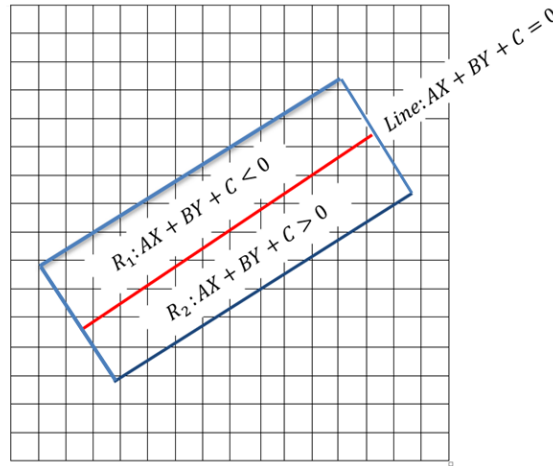


Figure 4.11: Line-support region W with its corresponding line that divides the region into R_1 and R_2 .

Suppose W be a line-support region with corresponding line

$$AX + BY + C = 0 \quad (4.31)$$

The line divides the line-support region W into two regions R_1 and R_2 (Figure 4.11): the region in one side of the line with

$$AX_i + BY_i + C < 0 \quad (4.32)$$

and the region on the other side of the line with

$$AX_i + BY_i + C > 0 \tag{4.33}$$

That is

$$R_1 = \{(X_i, Y_i) \in W: AX_i + BY_i + C < 0\}$$

$$R_2 = \{(X_i, Y_i) \in W: AX_i + BY_i + C > 0\} .$$

The average intensities on both regions are calculated by

$$\bar{f}_1 = \frac{1}{M} \sum_{(X_i, Y_i) \in R_1} f(X_i, Y_i) \tag{4.34}$$

$$\bar{f}_2 = \frac{1}{N} \sum_{(X_i, Y_i) \in R_2} f(X_i, Y_i) \tag{4.35}$$

where $f(X_i, Y_i)$ is the intensity value at pixel (X_i, Y_i) , M and N are the number of pixels in R_1 and R_2 respectively. Then contrast of the edge is calculated by

$$Contrast = \bar{f}_2 - \bar{f}_1 \tag{4.36}$$

and steepness of the edge is computed as

$$Steepness = \frac{Contrast}{width} \tag{4.37}$$

The procedure of edge strength determination is summarized in Figure 4.12.

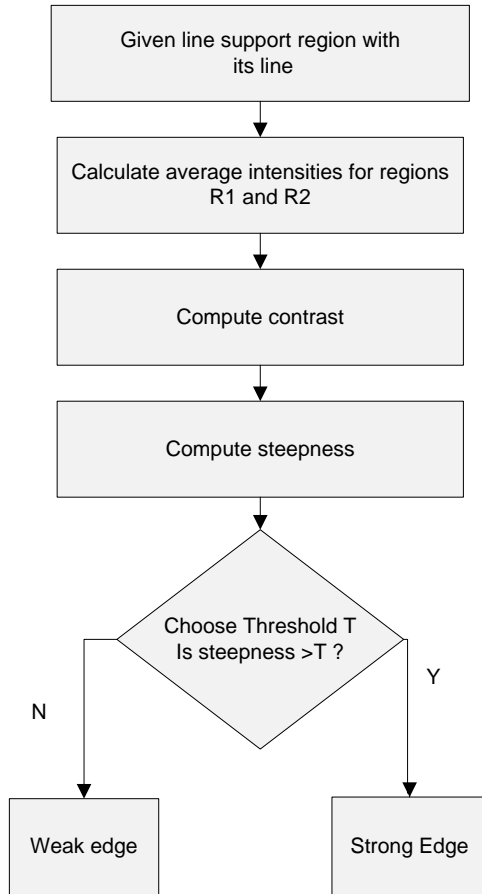


Figure 4.12: Steps in edge strength determination.

4.4.2. Validation and Accuracy Assessment

The automatically extracted line segments can be compared with the manually digitized boundaries of the reference data by adopting accuracy assessment methods proposed in literature. The method presented in this research is based on the method developed by Sidiropoulou Velidou et al. (2015), which uses the distance and orientation difference between the reference dataset and automatically extracted dataset. Here, instead of taking the local orientation difference of a pair of corresponding points, the orientation difference between the line segments where the two corresponding points lie is considered. Let l_1, l_2, \dots, l_m be the detected line segments with orientations $\alpha_1, \alpha_2, \dots, \alpha_m$ respectively. To assess the level of correspondence between these detected line segments with the reference dataset, the following steps are followed.

Steps:

1. Set distance thresholds d_r, d_e and angle threshold θ_0 .
2. Approximate the reference polygons by a set of local straight line segments and label them m_1, m_2, \dots, m_n and compute their corresponding orientations: $\beta_1, \beta_2, \dots, \beta_n$.
3. For each line segment in step 2, take sample points at an interval equal to the pixel spacing over its entire extent.
4. Determine corresponding points between reference line segments and detected line segments. Two points are considered to be corresponding points if they are close and the line segments where these points lie share similar orientation. These measures are applied starting from reference to detection and vice versa. Thus, two points are considered to be corresponding if the following conditions are satisfied.

$$a. \quad S < d_{r,e} \tag{4.38}$$

$$b. \quad |\alpha - \beta| < \theta_0 \tag{4.39}$$

where S is the Euclidean distance between the two points, and α is the orientation of the detected line segment where the first point lies and, β is the orientation of the reference line segment where the corresponding point lies. These orientation angles were transformed into the range $[0, \pi]$ and orientations with a difference of π were considered parallel.

From reference to detection

If there exists a corresponding point for the interval point of the reference line, then this is considered as successful detection. If not, such point is considered as a missing one.

The ratio of missing (RM) and Ratio of successful detections (RS_r) are defined as follows:

$$RM = \frac{\text{total number of interval points with no correspondence}}{\text{total number of interval points}} \tag{4.40}$$

$$RS_r = 1 - RM \tag{4.41}$$

Low RM value would imply that many points in the reference dataset have corresponding points in the detected dataset. That is, low value of RM implies high successful detection. RM and RS_r measure the completeness of the result with respect to reference dataset.

From detection to reference

The same procedures are repeated from detected points to the interval points of the reference lines.

If there exists a corresponding interval point for the detected point, then this is considered as successful detection. If not, this detected point is false detection. The ratio of false detection (RF) and ratio of successful detections (RS_e) are given by:

$$RF = \frac{\text{total number of detected points with no correspondence}}{\text{total number of detected points}} \quad (4.42)$$

$$RS_e = 1 - RF \quad (4.43)$$

High RF would imply a deviation in either the position or the orientation of the detected dataset from the reference dataset. The RF and RS_e measure the correctness of the result.

Positional Accuracy

To assess the positional accuracy of successful detections, mean and standard deviation of the distances of corresponding points were computed. These values show the positional shift between the reference and detected dataset in terms of distance.

4.4.3. Parameter tuning

In order to select the best set of data that have better extracted line segments using LSD algorithm, the four parameters: scale (S), gradient magnitude threshold (ρ), angle tolerance (τ) and detection threshold (ε) were considered. The tuning process was performed individually by varying the values of one parameter over a certain range and keeping the other parameters fixed. The order of the tuning was based on their occurrence in the algorithm. The evaluation of the results was based on the minimization of the sum of RM and RF and giving balance between RM and RF as much as possible. First the parameter S was tuned by keeping the other three parameters fixed to their default values. After the tuning of S , the second and third parameters tuned were ρ and τ respectively. The tuning of ε was performed at last. The tuning process was performed twice on two different datasets. The first was performed on a small subset of multispectral satellite imagery (acquired on 29 July 2014) from study area Mali for the purpose of field boundary delineation and the second was performed on a panchromatic image from Nigeria (acquired on 12 September 2015) for the purpose of crop row detection. In the tuning process, for farm field delineation, the distance thresholds (Equation 4.38) were set to 3 m (which is close to 2.4 m, the minimum acceptable standard accuracy level in rural areas set by the International Association of Assessing Officers) (Officers, 2012) and angle threshold was set to $\pi/8$. For crop row detection, the distance thresholds were set to 0.75 m and the angle threshold was set to $\pi/16$. The tuning results of these parameters are presented in chapter 5.

5. RESULTS

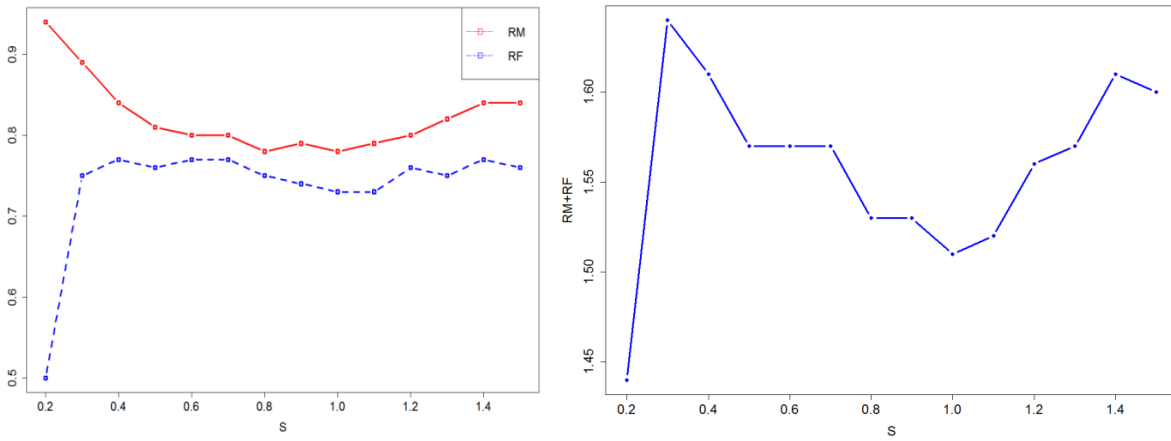
5.1. Farm field delineation

5.1.1. Tuning of S

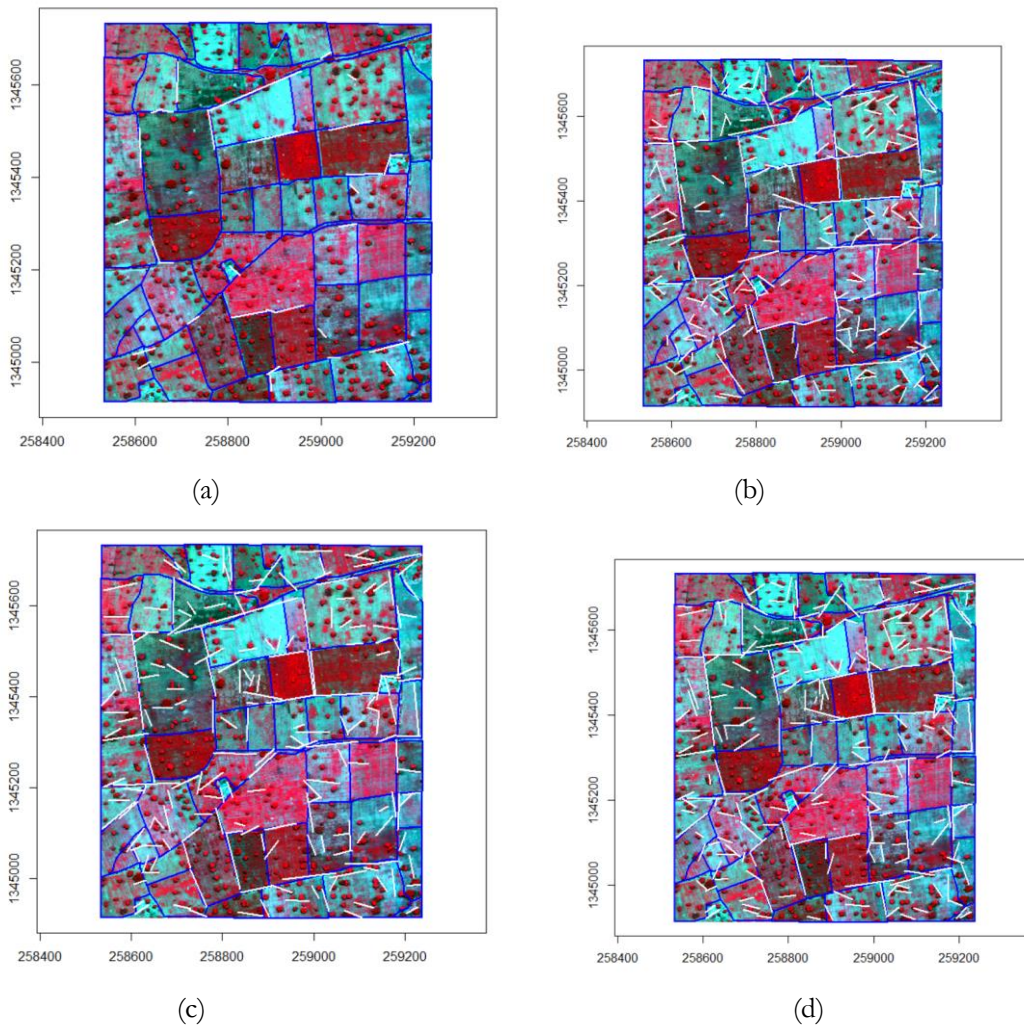
By fixing the two parameters $\tau = 22.5^\circ$ and $\varepsilon = 1$ (Grompone von Gioi et al., 2012), scale values in the range [0.2, 1.5] at an interval of 0.1 were tested to see the patterns of ratio of missing detection (RM) and ratio of false detection (RF). The second and third columns of Table1 show the patterns of RM and RF for varying scale. For these scale values, both RM and RF showed small variations in narrow ranges. RM varied from 0.78 to 0.94 whereas RF varied from 0.50 to 0.77. For $S \in [0.2, 1]$, RM followed a decreasing pattern (Figure 5.1a) except at $S = 0.8$ but RF followed an increasing pattern from $S = 0.2$ to $S = 0.4$ and showed small variations between $S = 0.5$ and $S = 1.0$. For $S > 1$, RF generally followed an increasing pattern, but RF oscillated between values of 0.73 and 0.7. The minimum value of RM was observed at $S = 0.8$ and $S = 1.0$. Both RM and RF are high for all scale values in the tested interval. It was observed that RM is slightly higher than RF for all scale values. Figure 5.1b shows the graph of $RM + RF$ for varying scale parameter. The minimum $RM + RF$ was observed at $S = 0.2$, followed by $S = 1.0$. Though the minimum sum was observed at $S = 0.2$, there was no balance between RM and RF. Only very few detections were observed at this S value (Figure 5.2a). Thus, the other S value that minimized the sum $RM + RF$ was $S = 1.0$. There was relatively balance between $RM = 0.78$ and $RF = 0.73$ at $S = 1.0$. Thus, $S = 1.0$, which corresponds to the scale of the original image, was selected as an optimum value. The detection results for selected S values are presented in Figure 5.2.

Table 5.1: RM and RF for varying S for fixed $\varepsilon = 1$ and $\tau = 22.5^\circ$.

S	RM	RF	RM+RF	Average distance between points (m)		Standard deviation of distance	
				Det. to Ref.	Ref. to Det.	Det. to Ref.	Ref. to Det.
0.2	0.94	0.5	1.44	1.7	1.69	0.82	0.83
0.3	0.89	0.75	1.64	1.62	1.62	0.78	0.79
0.4	0.84	0.77	1.61	1.59	1.58	0.77	0.77
0.5	0.81	0.76	1.57	1.67	1.66	0.75	0.75
0.6	0.8	0.77	1.57	1.61	1.61	0.76	0.76
0.7	0.8	0.77	1.57	1.54	1.53	0.76	0.76
0.8	0.78	0.75	1.53	1.49	1.48	0.8	0.79
0.9	0.79	0.74	1.53	1.52	1.51	0.76	0.77
1.0	0.78	0.73	1.51	1.49	1.48	0.72	0.73
1.1	0.79	0.73	1.52	1.48	1.46	0.71	0.71
1.2	0.80	0.76	1.56	1.48	1.48	0.73	0.73
1.3	0.82	0.75	1.57	1.54	1.54	0.73	0.73
1.4	0.84	0.77	1.61	1.56	1.54	0.76	0.77
1.5	0.84	0.76	1.6	1.58	1.55	0.74	0.73



(a) (b)
 Figure 5.1(a) Ratio of missing(RM) and ratio of false (RF) detections, (b) RM+RF for varying scale parameter S for fixed $\tau = 22.5^\circ$ and $\varepsilon = 1$. The low S value would imply coarse spatial resolution and large S value would imply fine spatial resolution.



(a) (b) (c) (d)
 Figure 5.2: Detection results for different S values. (a) S = 0.2 , (b) S = 0.5 , (c) S = 0.8, (d) S = 1.0. Blue segments: reference segments, white: detected segments. For the image displayed: R = 7, G = 5, B = 3.

Mean distance and standard deviations between corresponding points

The mean distance and standard deviation from points of the detected data set to the corresponding sample points of the reference dataset were calculated. These statistical measures were also computed in the opposite direction, from reference points to detected points. The results are presented in Table 5.1. These distance values and standard deviations reflect the positional accuracy of successful detections. That is the distance values show the positional shift between the reference and detected segments. Higher distance values indicate higher deviation of the detected line segments from the reference segments. As can be seen from Figure 5.3, the distance values vary depending on the scale parameter. At lower values of S , the deviation is higher. Relatively lower distance values were observed between $S=0.8$ and $S=1.2$.

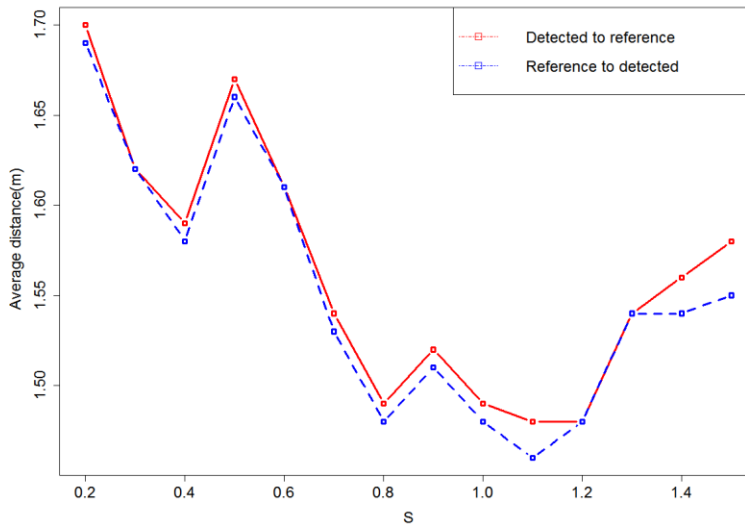


Figure 5.3: Distance between points for varying the value of S

Contrast and steepness of detected line segments

Figure 5.4 (a) -(d) show box plots of contrast and steepness of both successful detection and false detection of segments for $S = 1$, $\tau = 22.5^\circ$ and $\varepsilon = 1$. Box plots (a) and (b) show the distribution of contrast for true detection and false detection respectively. In these box plots, it is observed that the mean contrast of segments for true detections is higher than the mean contrast of segments of that of false detections. Box plots (c) and (d) show the distribution of the steepness of segments of both successful detections and false detections respectively. From the box plots it is observed that the mean steepness of line segments of true detections is greater than the mean steepness of segments of false detections. Thus, these attributes (contrast and steepness) could help for further processing as they rank edges according to their strength.

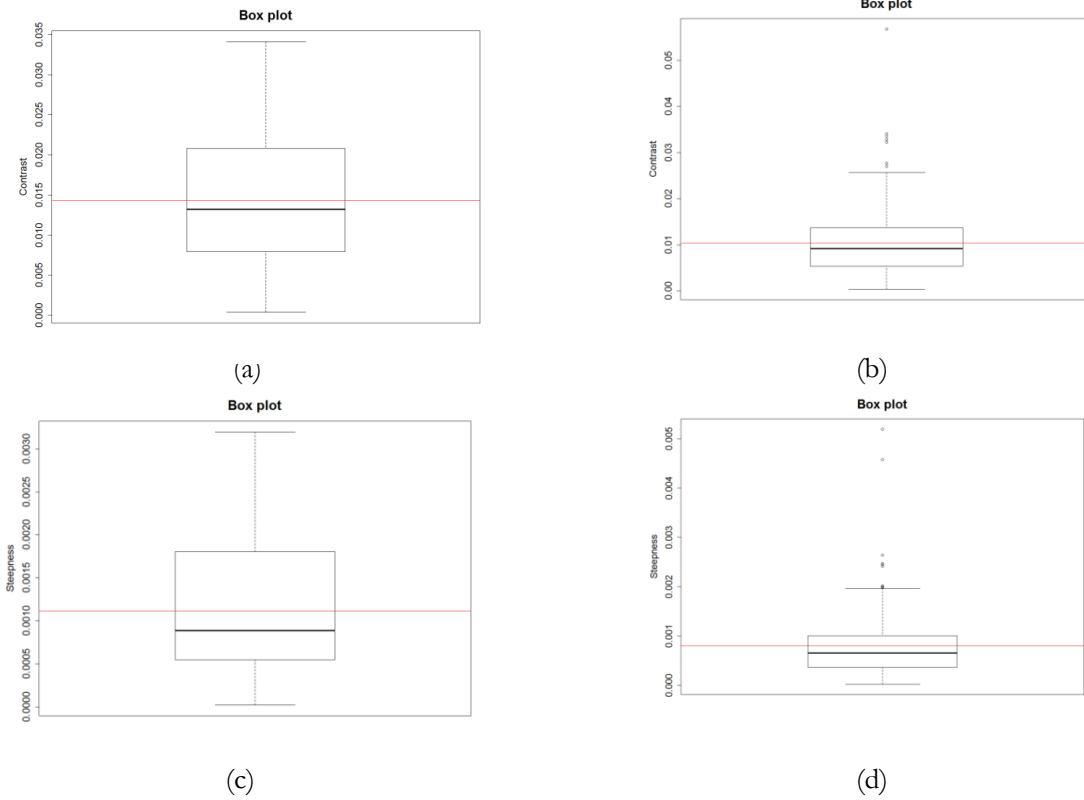


Figure 5.4: Box plots showing distributions of contrast and steepness of true detections and false detections. (a) Contrast of successful detections, (b) Contrast of false detections, (c) Steepness of true detections, (d) Steepness of false detections.

5.1.2. Tuning of gradient magnitude threshold ρ

To see the patterns of RM and RF on varying the values of ρ , the other parameters S , τ and ε were kept fixed at values 1.0, 22.5° and 1.0 respectively. The threshold ρ is determined by the formula given in Equation 4.17. Usually, the parameter q , a bound on the possible error in the gradient value due to quantization noise, was set to 2 (Grompone von Gioi et al., 2012). Different q values were tested to see the pattern of RM and RF. The results are presented in Table 5.2. For $q < 2$, there were almost no changes observed of the values of both RM and RF. But RF decreased rapidly when q increased to 4. However, there were only very few detections observed as the value of q increased. Thus, $q = 2$ is a good choice as suggested in the literature.

Table 5.2: RM and RF for varying gradient magnitude threshold for fixed $S = 1$, $\tau = 22.5^\circ$ and $\varepsilon = 1$.

q	RM	RF	RM+RF
0.005	0.77	0.87	1.64
0.05	0.77	0.87	1.64
0.5	0.77	0.87	1.64
1	0.77	0.83	1.60
2	0.78	0.73	1.51
3	0.82	0.62	1.44
4	0.87	0.51	1.38

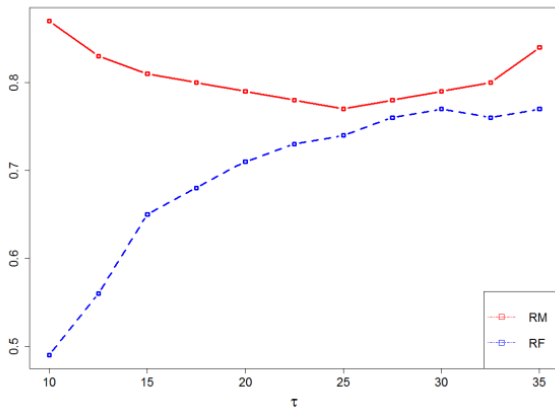
5.1.3. Tuning of angle tolerance

The third parameter to be tuned was τ . For this tuning, S and ϵ were both fixed at value of 1.0 and the quantization q for gradient threshold was set to 2. The values of τ between 10° and 35° at an interval of 2.5° were tested. The results are presented in Table 5.3. For τ between 10° and 25° , RM followed a decreasing pattern, reaching its minimum value 0.77 at $\tau = 25^\circ$. But it followed an increasing pattern for $\tau > 25^\circ$ (Figure 5.5a). On the other hand, RF generally followed an increasing pattern as τ moves from lower to higher values. Figure 5.5b presents the graph of RM +RF for varying τ . The minimum value of

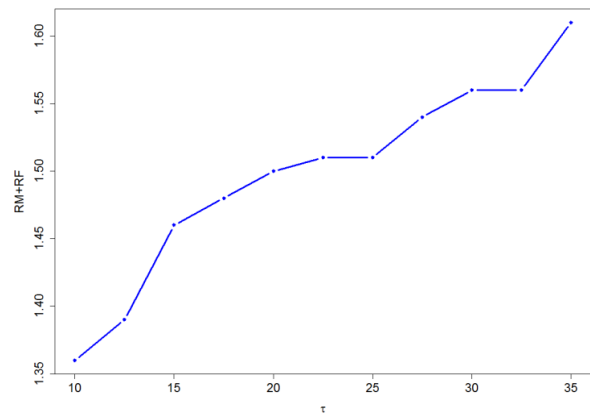
Table 5.3: RM, RF, Average distance and standard deviation between corresponding points for varying τ for fixed $S=1.0$ and $\epsilon=1$.

τ (Degree)	RM	RF	RM+RF	Average distance between points (m)		Standard deviation of distance	
				Det. to Ref.	Ref to Det.	Det. to Ref.	Ref. to Det.
10	0.87	0.49	1.36	1.47	1.48	0.72	0.73
12.5	0.83	0.56	1.39	1.46	1.47	0.71	0.72
15	0.81	0.65	1.46	1.51	1.51	0.72	0.72
17.5	0.80	0.68	1.48	1.48	1.48	0.73	0.73
20	0.79	0.71	1.5	1.51	1.50	0.74	0.73
22.5	0.78	0.73	1.51	1.49	1.48	0.72	0.73
25	0.77	0.74	1.51	1.51	1.50	0.73	0.73
27.5	0.78	0.76	1.54	1.50	1.50	0.72	0.73
30	0.79	0.77	1.56	1.50	1.50	0.73	0.73
32.5	0.80	0.76	1.56	1.51	1.51	0.73	0.74
35	0.84	0.77	1.61	1.56	1.56	0.74	0.75

the sum was observed at $\tau = 10^\circ$. However, visual inspection showed that there were only few detections at this τ value. RM+RF was almost stable between $\tau = 20^\circ$ and $\tau = 25^\circ$. So one value from these three values could be selected. The value $\tau = 22.5^\circ$ was selected as optimum value (average distance between corresponding points is lower for this value than the other two). Detection results for different τ values are presented in Figure 5.6.



(a)



(b)

Figure 5.5 (a) Ratio of missing (RM) and ratio of false (RF) detections, (b) RM+RF for varying τ for fixed $S = 1.0$ and $\epsilon = 1.0$.

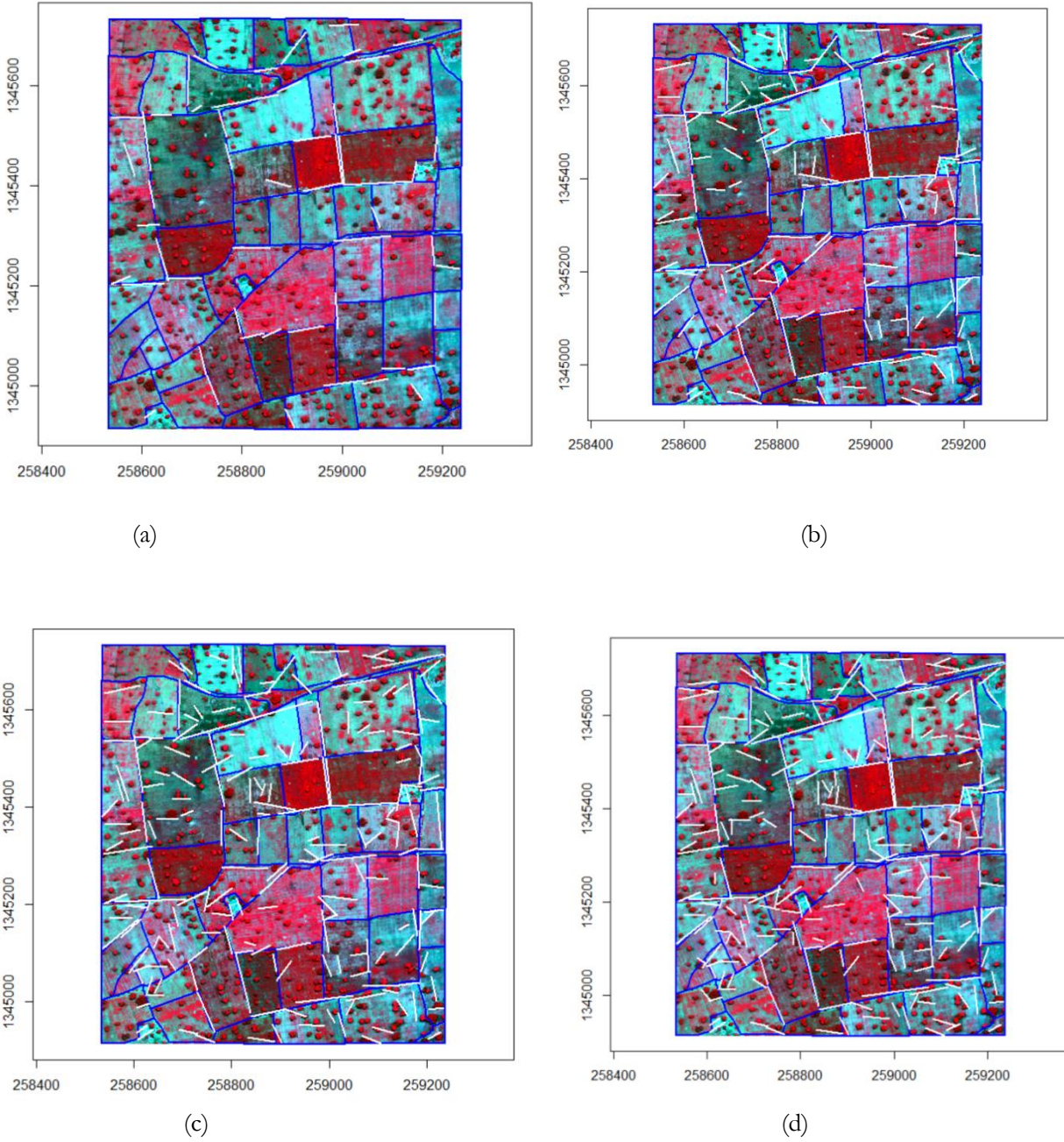


Figure 5.6: Detection results for different τ values for fixed values $S = 1.0$, $\varepsilon = 1.0$ (a) $\tau = 10^\circ$, (b) $\tau = 17.5^\circ$, (c) $\tau = 22.5^\circ$, (d) $\tau = 25^\circ$. Blue segments are reference segments, white segments are detected segments. For image displayed $R=7$, $G=5$, $B=3$.

5.1.4. Tuning of detection threshold epsilon (ϵ)

The last parameter to be tuned was the detection threshold ϵ . Usually the value of this detection threshold is set to 1 without any further experiment (Desolneux et al., 2003). In order to decide whether $\epsilon = 1$ is indeed the optimal value for this application and to check the stability of the results, different detection threshold values above and below 1.0 were tested. The scale parameter was fixed to $S = 1$ and the angle tolerance was fixed to $\tau = 22.5^\circ$. As can be seen from Table 5.4, generally, RM values are higher for $\epsilon < 1$ than RM values for $\epsilon > 1$. The opposite happens for RF. Low ϵ values mean strict threshold, which allows only more meaningful segments to pass the NFA control. Both RM and RF are stable for values of ϵ between 0.5 and 10. Any value in this interval can be selected as optimal value. However, in order not to accept many segments that could randomly occur in the image, the value of ϵ is set to 1.0.

Table 5.4: RM and RF for varying detection threshold ϵ for fixed $S = 1.0$ and $\tau = 22.5^\circ$.

ϵ	RM	RF	RM+RF	Average distance between points (m)		Standard deviation of distance	
				Det. to Ref.	Ref. to Det.	Det. to Ref.	Ref. to Det.
10^{-40}	0.95	0.60	1.55	1.46	1.45	0.67	0.67
10^{-10}	0.82	0.67	1.49	1.50	1.50	0.74	0.73
0.1	0.79	0.71	1.50	1.51	1.50	0.74	0.73
0.5	0.79	0.71	1.50	1.51	1.50	0.74	0.73
1	0.78	0.73	1.51	1.51	1.50	0.74	0.73
5	0.78	0.73	1.51	1.49	1.48	0.72	0.73
10	0.78	0.73	1.51	1.49	1.48	0.72	0.73
50	0.78	0.74	1.52	1.49	1.48	0.72	0.73
10^{40}	0.78	0.74	1.52	1.49	1.48	0.73	0.73

Results after parameter tuning

After tuning all the three parameters individually, the optimum values of the parameters selected were $S=1$, $\tau = 22.5^\circ$ and $\epsilon = 1$. For these selected parameter values, the ratio of missing and the ratio of false detections obtained were $RM = 0.78$ and $RF = 0.73$ respectively. The resulting image, successful detections from reference to detection and detection to reference are shown in Figures 5.7- 5.9.

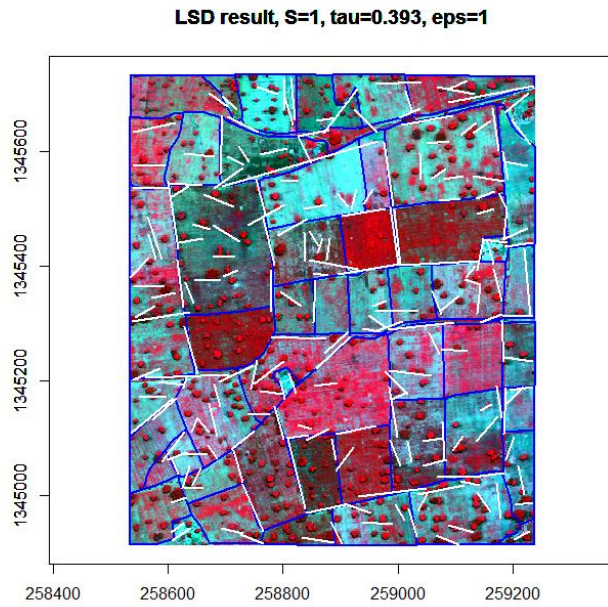


Figure 5.7: Detected line segments with reference dataset on image band (blue segments are reference segments, white segments are detected segments, $R=7$, $G=5$, $B=3$) for $S=1$, $\tau=22.5^\circ$ and $\epsilon=1$.

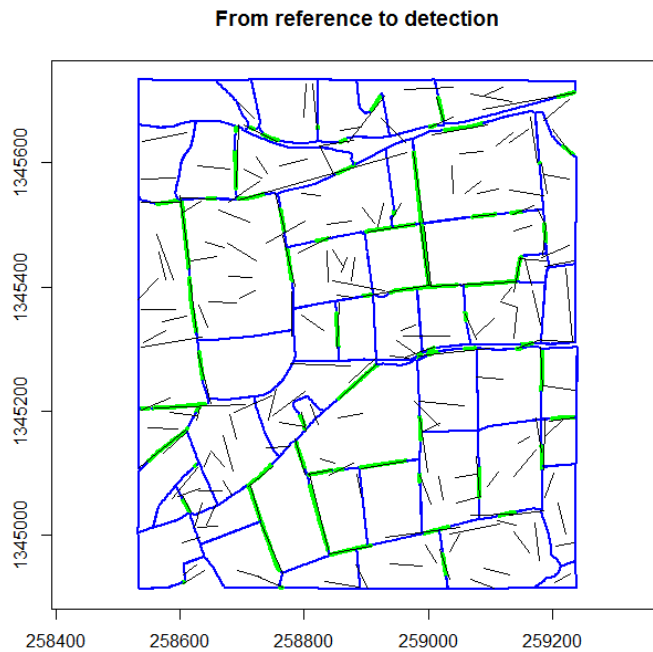


Figure 5.8: Successful detections from reference to detection for $S=1$, $\tau = 22.5^\circ$, $\epsilon = 1$. Blue segments are reference segments, black segments are detected segments, green segments show successful detections.

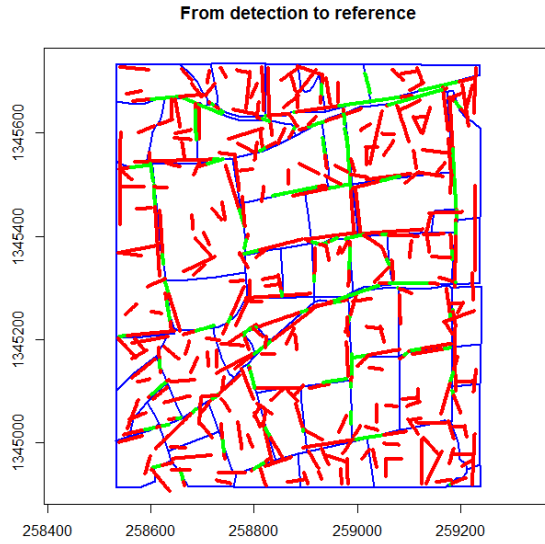


Figure 5.9: Successful detections from detection to reference for $S=1$, $\tau=22$, 5° , $\epsilon=1$. Blue segments are reference segments, red segments are detected segments, green segments show successful detections.

Results of LSD on Texture Bands

The eight second order texture measures were tested for three different spatial distance values ($d = 1, 2, 3$ pixels) in four different directions ($0^\circ, 45^\circ, 90^\circ, 135^\circ$). The window size used for GLCM calculation was 5×5 . Comparison of the results among these texture measures was performed in terms of RM and RF values. The three texture measures which yielded relatively better results are GLCM contrast, GLCM mean and GLCM variance. The RM and RF values of these three texture measures for three spatial distance values in the horizontal direction are presented in Table 5.5. As can be seen from the Table, both RM and RF are very high for all three GLCM texture measures. For GLCM contrast, there are slight variations in the values of RM and RF for different distance values (Figure 5.10a). For GLCM mean and GLCM contrast, varying the spatial distance has almost no effect on the RM and RF (Figure 5.10 (b) & (c)). GLCM variance has low RM and RF values as compared to both GLCM mean and GLCM contrast. Detected results of LSD applied on GLCM contrast for $d = 3$ in the horizontal direction is shown in Figure 5.11 and detection results for GLCM mean and GLCM contrast results for $d = 3$ in the horizontal direction are presented in Appendix (B). For GLCM mean $RM > RF$, but only a few line segments were detected.

Table 5.5: RM and RF for three spatial distance values

Texture Measure	Distance (d)	RM	RF
GLCM contrast	1	0.85	0.87
	2	0.83	0.90
	3	0.82	0.90
GLCM mean	1	0.96	0.86
	2	0.96	0.86
	3	0.96	0.86
GLCM variance	1	0.79	0.83
	2	0.79	0.83
	3	0.79	0.83

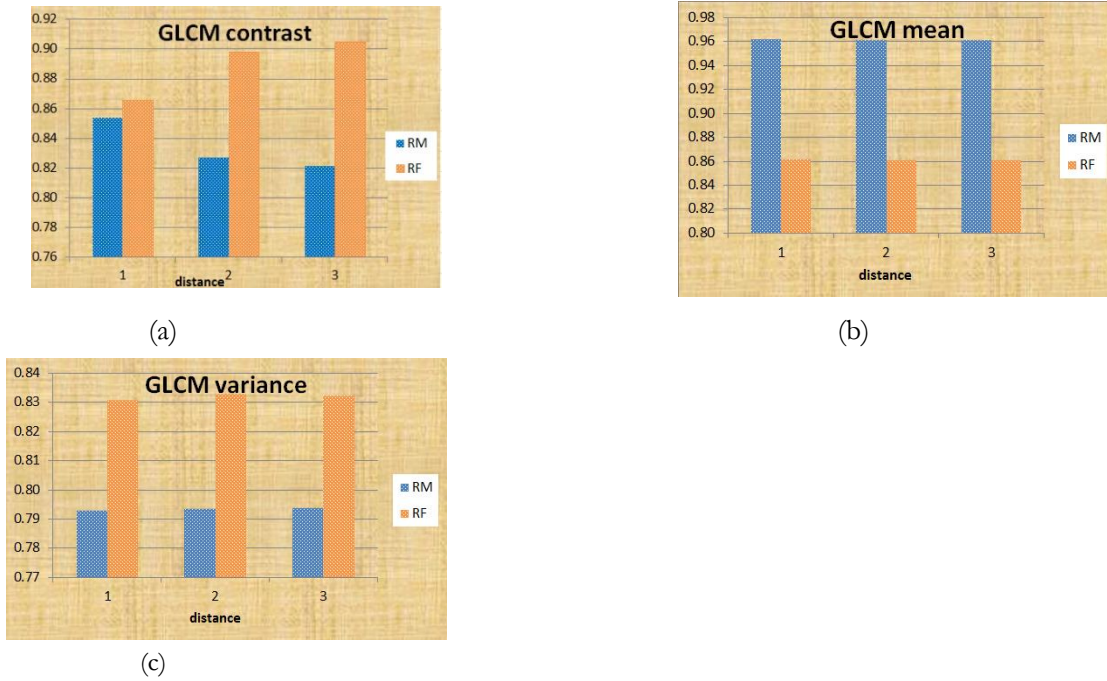


Figure 5.10: RM and RF for three spatial distance values in the horizontal direction. (a) GLCM contrast, (b) GLCM mean, (c) GLCM variance.

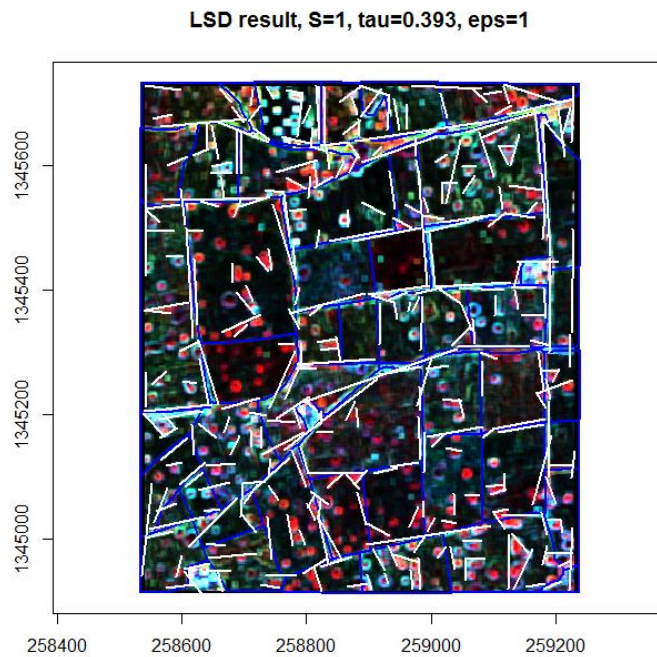


Figure 5.11: Detected line segments with reference dataset on texture band (GLCM contrast for $d = 3$ in the horizontal direction) for $S=1$, $\tau = 22.5^\circ$, $\epsilon = 1$. Blue segments are reference segments, white segments are detected segments, $R=7$, $G=5$, $B=3$.

5.2. Parameter tuning for crop rows detection

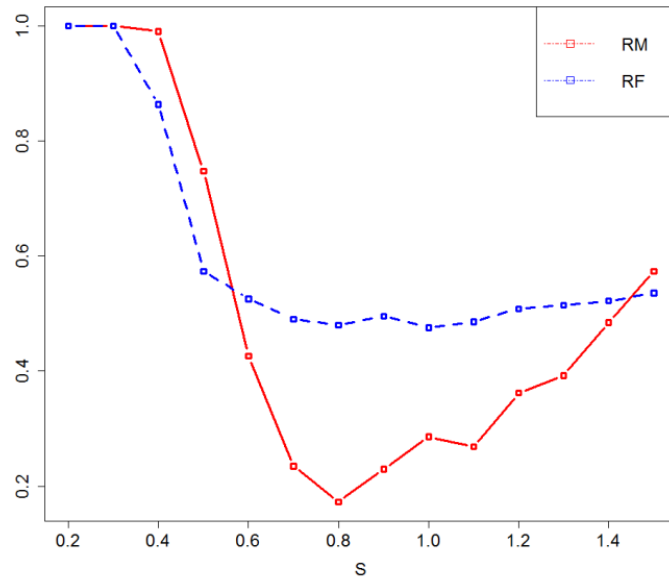
5.2.1. Tuning of S

As in section 5.1, the first parameter to be tuned was scale parameter S. Values of S between 0.2 and 1.5 at an interval of 0.1 were experimented by fixing $\tau = 22.5^\circ$ and $\varepsilon = 1$. The results are presented in Table 5.6. RM showed higher variation than RF. The range at which RM and RF varied were [0.17, 1] and [0.48, 1] respectively. The maximum values of RM and RF were observed at $S = 0.2$ and $S = 0.3$. At these S values, visual inspection showed that the algorithm detected very few line segments. The minimum value of RM was 0.17 which was observed at $S = 0.8$ and the minimum value of RF was 0.48 which was observed at $S = 0.8$ and $S = 1.0$. For $S \in [0.2, 0.8]$, both RM and RF followed a decreasing pattern as can

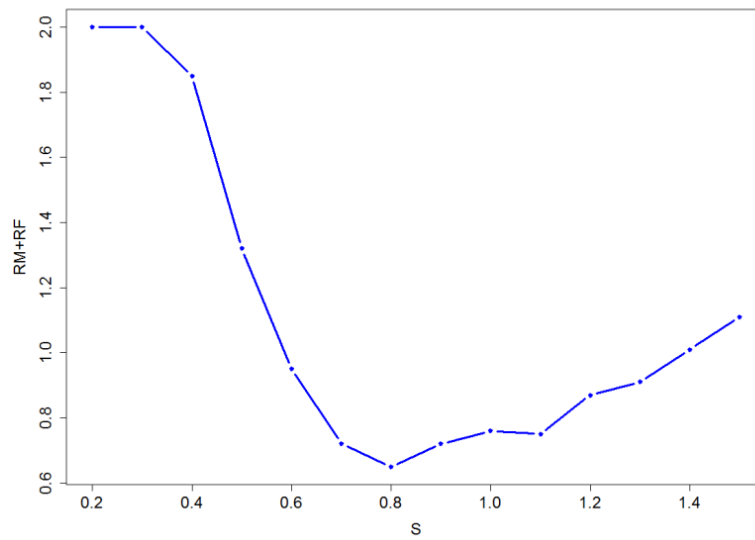
Table 5.6: RM and RF for varying S for fixed $\tau = 22.5^\circ$ and $\varepsilon = 1$.

S	RM	RF	RM+RF	Average distance between points (m)		Standard deviation of distance	
				Det. to Ref.	Ref. to Det.	Det. to Ref.	Ref. to Det.
0.2	1.00	1.00	2.00	-	-	-	-
0.3	1.00	1.00	2.00	-	-	-	-
0.4	0.99	0.86	1.85	0.34	0.36	0.17	0.18
0.5	0.75	0.57	1.32	0.41	0.41	0.18	0.18
0.6	0.43	0.53	0.95	0.37	0.36	0.19	0.18
0.7	0.23	0.49	0.72	0.37	0.34	0.19	0.18
0.8	0.17	0.48	0.65	0.37	0.34	0.18	0.17
0.9	0.23	0.50	0.72	0.38	0.35	0.18	0.17
1.0	0.29	0.48	0.76	0.38	0.34	0.19	0.17
1.1	0.27	0.49	0.75	0.40	0.36	0.18	0.17
1.2	0.36	0.51	0.87	0.39	0.36	0.18	0.18
1.3	0.39	0.51	0.91	0.41	0.38	0.19	0.19
1.4	0.48	0.52	1.01	0.40	0.37	0.19	0.19
1.5	0.57	0.54	1.11	0.41	0.39	0.19	0.19

be seen in Figure 5.12a. But for $S > 0.8$, RM followed an increasing pattern with an exception at $S = 1.1$. RF was relatively stable for $S > 0.8$. Figure 5.12b shows RM+RF for S values between 0.2 and 1.5. At this interval, the minimum and maximum values of RM+RF were 0.65 and 2.0 respectively. This large range of RM+RF shows the sensitivity of the result to variation of parameter S. The value of S which yielded the minimal sum of error RM+RF=0.65 was 0.8 and this value was selected as an optimum value. The detection results for two different S values are shown in Figure 5.13. These two detection results show how the scale parameter is critical on detection results.



(a)



(b)

Figure 5.12 (a) Ratio of missing(RM) and ratio of false(RF) detections, (b) RM+RF for varying scale parameter S for fixed $\tau = 22.5^\circ$ and $\varepsilon = 1$. The low S value would imply coarse spatial resolution and large S value would imply fine spatial resolution. An optimum value is observed at $S = 0.8$

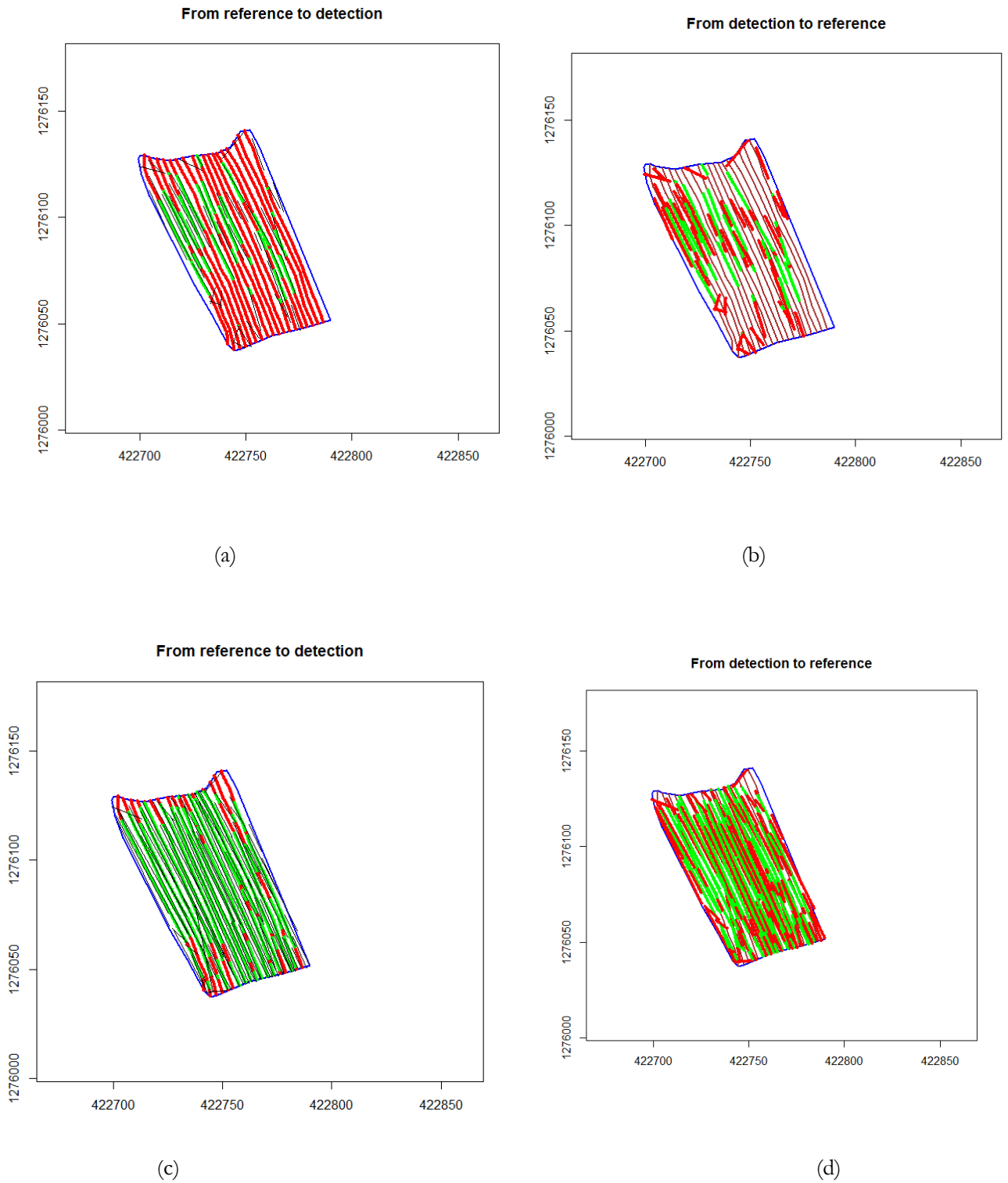


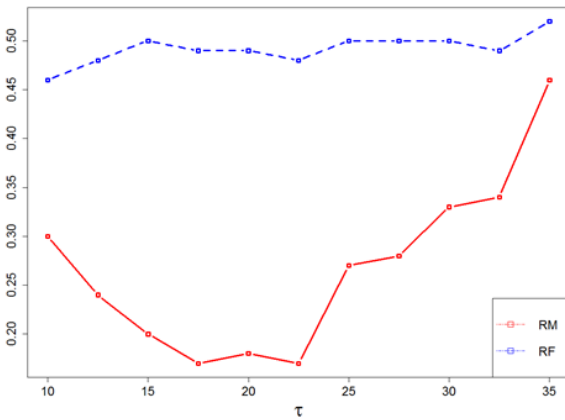
Figure 5.13: Successful detections for two different S values. Green: successful detection. (a) Successful detections from reference to detection for $S = 0.5$, (b) Successful detections from detection to reference for $S = 0.5$, (c) Successful detections from reference to detection for $S = 0.8$, (d) Successful detections from detection to reference for $S = 0.8$. Detection results are better for (c) and (d) than (a) and (b). which shows the influence of scale parameter on detection results

5.2.2. Tuning of τ

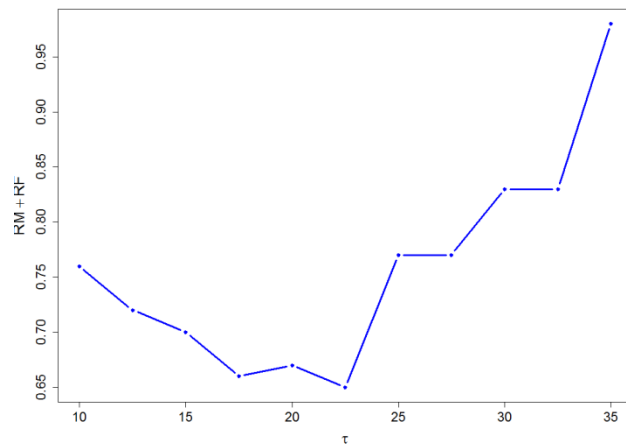
To see the patterns of RM and RF on varying the values of τ , the values of S and ϵ were kept fixed at 0.8 and 1.0 respectively. Values of τ between 10° and 35° at an interval of 2.5° were tested. The results are presented in Table 5.7. For τ between 10° and 17.5° , RM followed a decreasing pattern. But it followed an increasing pattern for $\tau > 17.5^\circ$ except at $\tau = 22.5^\circ$ (Figure 5.14a). On the other hand, RF increased from 0.46 to 0.50 as τ moved from 10° to 15° and became almost stable for higher values τ . Figure 5.14b presents the graph of RM +RF for varying τ . The value of τ that minimized the sum M+RF was $\tau = 22.5^\circ$.and this value was selected as an optimum vlue.

Table 5.7: RM and RF for varying angle tolerance τ and for fixed values of S=0.8 and $\epsilon =1$.

τ (Degree)	RM	RF	RM+RF	Average distance between points (m)		Standard deviation of distance	
				Det. to Ref.	Ref to Det.	Det. to Ref.	Ref. to Det.
10	0.30	0.46	0.76	0.38	0.35	0.18	0.16
12.5	0.24	0.48	0.72	0.38	0.35	0.18	0.16
15	0.20	0.50	0.70	0.38	0.36	0.17	0.16
17.5	0.17	0.49	0.66	0.37	0.34	0.18	0.17
20	0.18	0.49	0.67	0.37	0.34	0.18	0.17
22.5	0.17	0.48	0.65	0.37	0.34	0.18	0.17
25	0.27	0.50	0.77	0.37	0.34	0.19	0.17
27.5	0.28	0.50	0.77	0.37	0.34	0.18	0.17
30	0.33	0.50	0.83	0.37	0.34	0.18	0.17
32.5	0.34	0.49	0.83	0.37	0.34	0.18	0.17
35	0.46	0.52	0.98	0.37	0.35	0.19	0.18



(a)



(b)

Figure 5.14: (a) Ratio of missing(RM) and ratio of false(RF) detections, (b) RM+RF for varying angle tolerance τ . Low τ values are more restrictive for region growing, which does not allow pixels with large differences in gradient orientation to be included in the same line-support region.

5.2.3. Tuning of detection threshold ϵ

The third parameter to be tuned was the detection threshold ϵ . RM followed a decreasing pattern as ϵ moved to higher values as expected (Table 5.8). The highest value of RF=51 was observed at the highest value of τ . Both RM and RF were stable between $\tau = 0.1$ and $\tau = 100$. Thus, $\epsilon = 1$ is an acceptable choice as an optimal value as suggested in the literature.

Table 5.8: RM and RF for varying detection threshold ϵ and for fixed values of $S=0.8$ and $\tau = 22.5^\circ$.

ϵ	RM	RF	RM+RF	Average distance between points (m)		Standard deviation of distance	
				Det. to Ref.	Ref. to Det.	Det. to Ref.	Ref. to Det.
10^{-20}	0.38	0.48	0.88	0.37	0.34	0.18	0.17
10^{-10}	0.30	0.47	0.77	0.37	0.34	0.18	0.17
0.001	0.24	0.49	0.72	0.37	0.34	0.18	0.17
0.01	0.23	0.49	0.72	0.37	0.34	0.18	0.17
0.1	0.21	0.49	0.70	0.37	0.35	0.18	0.17
0.5	0.17	0.48	0.66	0.37	0.35	0.18	0.17
1	0.17	0.48	0.65	0.37	0.34	0.18	0.17
2	0.17	0.48	0.65	0.37	0.34	0.18	0.17
10	0.17	0.48	0.65	0.37	0.34	0.18	0.17
50	0.17	0.48	0.65	0.37	0.34	0.18	0.17
100	0.17	0.48	0.65	0.37	0.34	0.18	0.17
10^{40}	0.13	0.51	0.64	0.37	0.33	0.18	0.17

Results after parameter tuning

After tuning all the three internal parameters individually, the optimum values of the parameters selected were $S=0.8$, $\tau = 22.5^\circ$ and $\epsilon = 1$. For these selected parameter values, the ratio of missing and the ratio of false detections are $RM = 0.17$ and $RF = 0.48$ respectively. The resulting image, successful detections from reference to detection and detection to reference are shown in Figures 5.15 - 5.17.

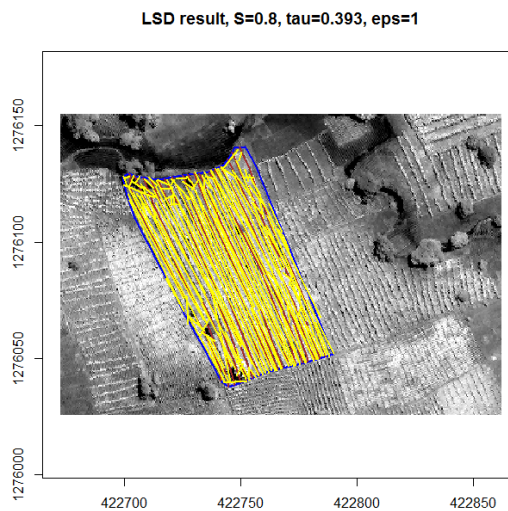


Figure 5.15: Detected results for optimum parameter values $S=0.8$, $\tau = 22.5^\circ$ and $\epsilon = 1$.

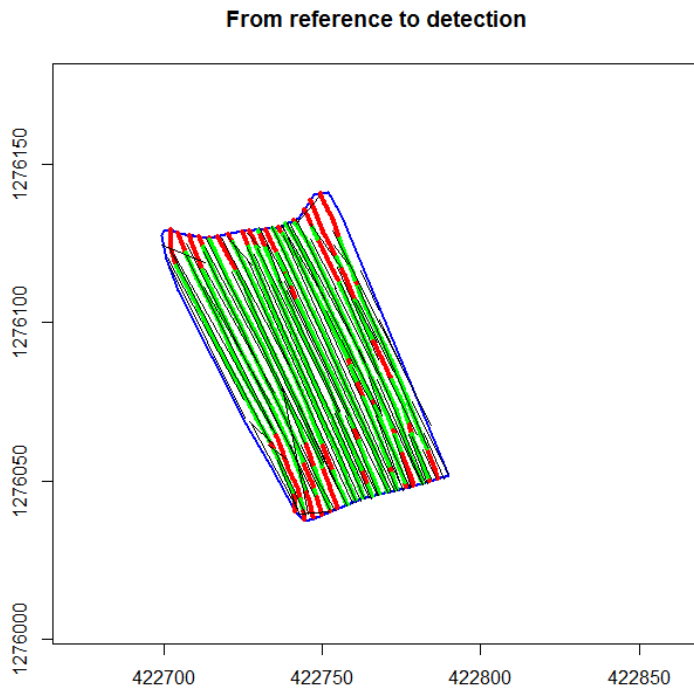


Figure 5.16: Successful detections from reference to detection for optimum parameter values $S=0.8$, $\tau=22.5^\circ$ and $\varepsilon=1$. Green color shows successful detections, red color shows missed detections, black lines are detected rows.

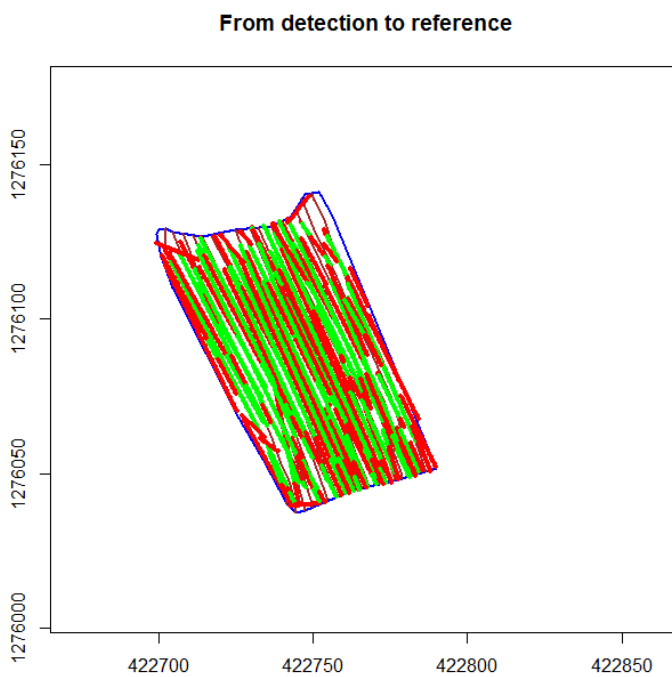


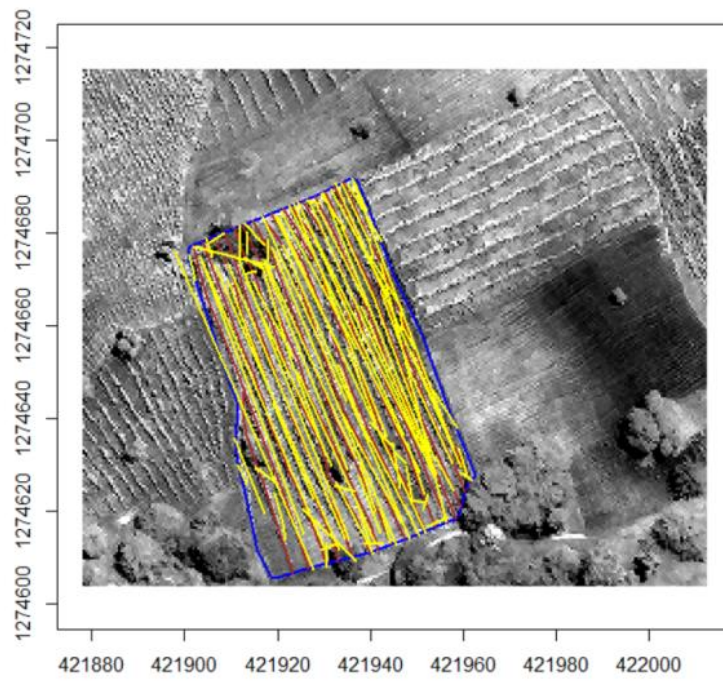
Figure 5.17: Successful detections from detection to reference for optimum parameter values $S = 0.8$, $\tau = 22.5^\circ$ and $\varepsilon = 1$. Green line segments show successful detections, red line segments show false detections.

5.3. Validation of the results of crop rows detection

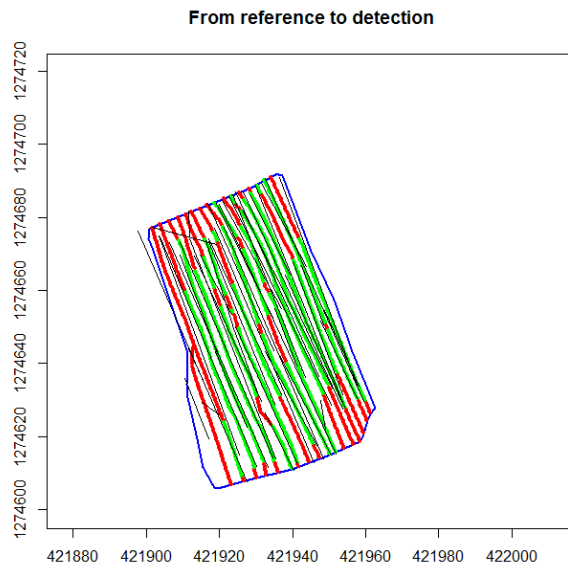
After fixing all parameter values, four subsets of the image of varying crop row width were selected to test the algorithm using the obtained parameter values. The number of crop rows in the selected subsets, including the subset for parameter tuning, ranges from 17 to 26. One additional subset of the image which has no crop rows was selected to check whether the algorithm reports false detections or not. The error ratios (RM and RF) for each subset are presented in Table 5.9 and the detection results of three subsets are presented in Figure 5.18-5.20. As can be seen from Table 5.9, ratios of missing detection (RM) of all subsets were higher than RM of the tuning subset. But ratios of false detections (RF) of two subsets (1 and 3) were lower than that of the tuning subset. RM is less than RF for all subsets. For most wide crop rows, the algorithm detected more than one segment for a single row. This caused relatively higher value of RF. For the selected subset with no crop rows, the algorithm didn't report detection results.

Table 5.9: RM and RF for different subsets for optimum parameter values $S = 0.8$, $\tau = 22.5^\circ$ and $\varepsilon = 1$.

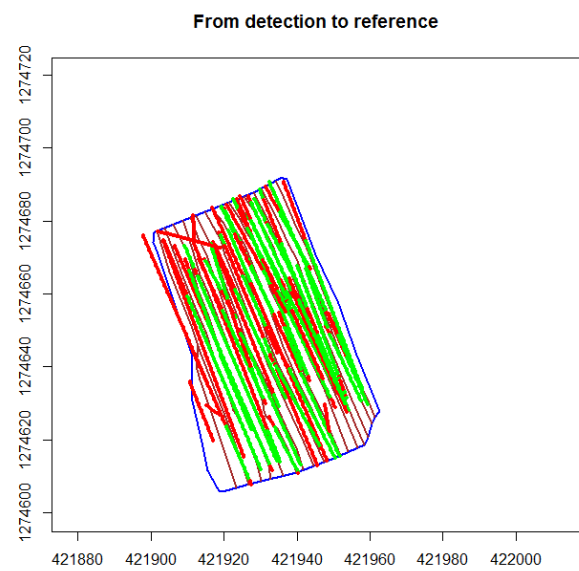
Subset	Region	RM	RF	Average distance between points (m)		Standard deviation of distance	
				Det. to Ref.	Ref. to Det.	Det. to Ref.	Ref. to Det.
1	roi_nig1	0.32	0.43	0.41	0.39	0.18	0.18
2	roi_nig4	0.42	0.50	0.36	0.35	0.17	0.17
3	roi_nig5	0.27	0.35	0.31	0.31	0.17	0.17
4	roi_nig6	0.53	0.75	0.48	0.48	0.18	0.18



(a)

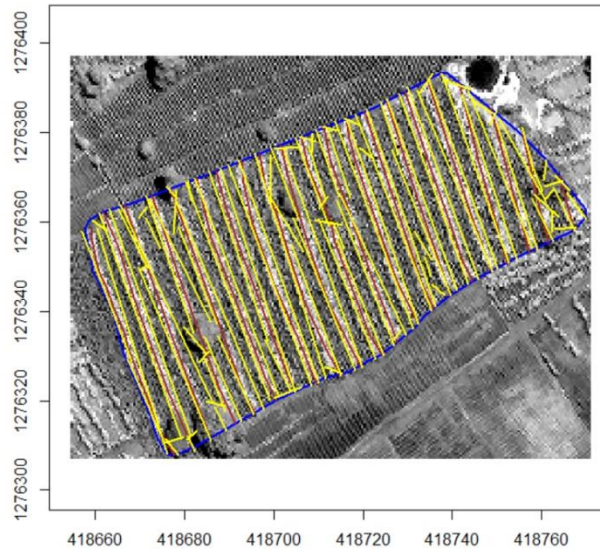


(b)

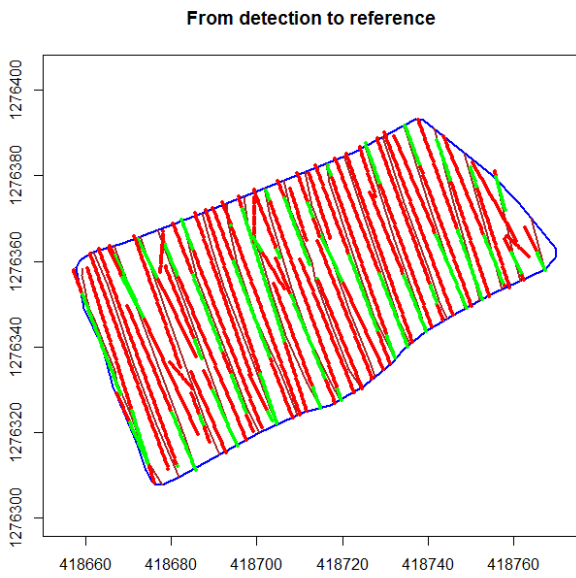


(c)

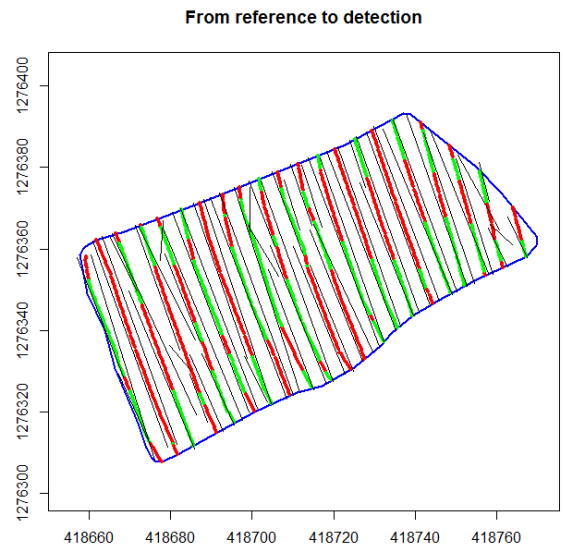
Figure 5.18: Results of Subset 1 for optimum parameter values $S=0.8$, $\tau=22.5^\circ$ and $\epsilon=1$. (a) Detected results, (b) Successful detections from reference to detection, (c) Successful detections from detection to reference.



(a)



(b)



(c)

Figure 5.19: Results of Subset 4 for optimum parameter values $S=0.8$, $\tau=22.5^\circ$ and $\epsilon=1$. (a) Detected results, (b) Successful detections from reference to detection, (c) Successful detections from detection to reference .

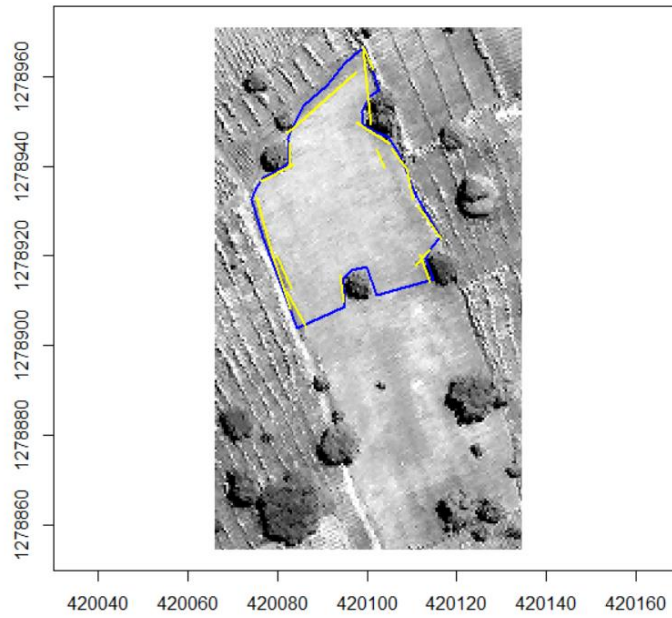


Figure 5.20: Detected results for optimum parameter values $S=0.8$, $\tau=22.5^\circ$ and $\epsilon=1$ of a field with no crop rows. No detection was reported in the field except near the boundaries of the field.

5.4. Dominant orientation of crop rows

Table 5.10 presents the number of crop rows and the dominant orientations for both the reference and detected dataset. As can be observed from the Table, the number of rows in the detected dataset is more than the number of rows in the reference data set. The algorithm detected more than one segment for a single row. Regarding the dominant orientation of the rows, the algorithm identified the dominant orientation of rows of each subset accurately. From the tested four subsets the algorithm identified the dominant orientations crop rows of three subsets only within a deviation of 0.57° from the reference. The maximum dominant orientation difference between the reference and the detected crop rows was 2.87° (subset 2). Figure 5.21 shows the rose diagram of the dominant row orientations of both the reference and detected datasets of selected subsets.

Table 5.10: Dominant orientation of crop rows and number of rows

Subset	Number of rows		Dominant orientation of rows (rad)		Dominant orientation difference between reference & detection	
	Reference	Detection	Reference	Detection	(In radians)	(In degree)
1	17	46	-1.15	-1.15	0	0
2	22	57	-0.87	-0.92	0.05	2.87
3	26	55	-1.09	-1.08	0.01	0.57
4	21	59	-1.22	-1.21	0.01	0.57

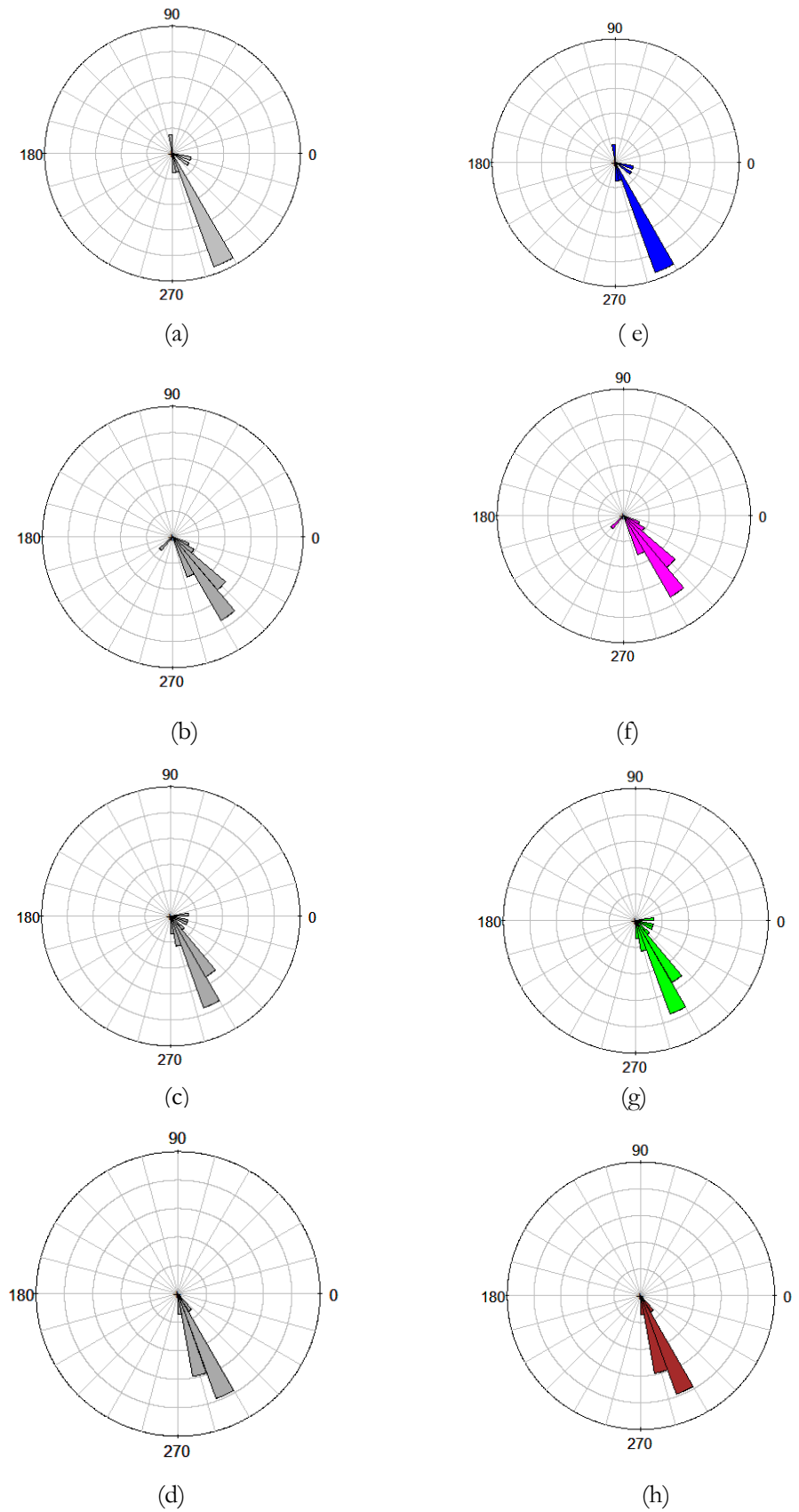


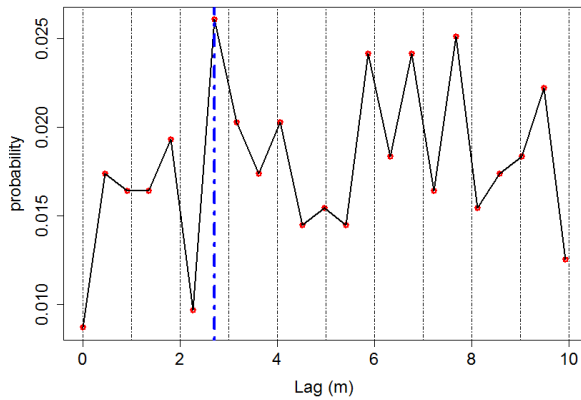
Figure 5.21: Rose diagram of dominant orientation of crop rows of both reference and detection for four validation subsets. (a-d) are the orientations of reference rows and (e-h) are the orientations of their corresponding detected rows of subsets 1-4 respectively.

5.5. Spacing of Crop rows

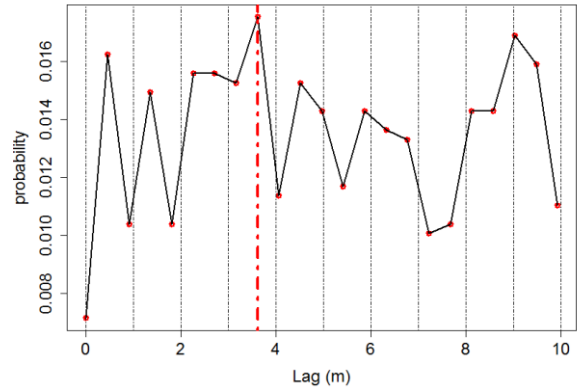
Table 5.11 presents the average spacing of crop rows for both reference and automatically detected datasets of four subsets. From the Table it is observed that the spacing between crop rows obtained by the proposed method for all subsets are higher than the reference datasets. The maximum crop row spacing difference between the reference dataset and the automatically detected dataset was 0.93 m (Subset 3) and the minimum was 0.03 m (subset 1). Figure 5.22 shows the spacing of crop rows obtained by applying the proposed procedure.

Table 5.11: Spacing of crop rows for four subsets.

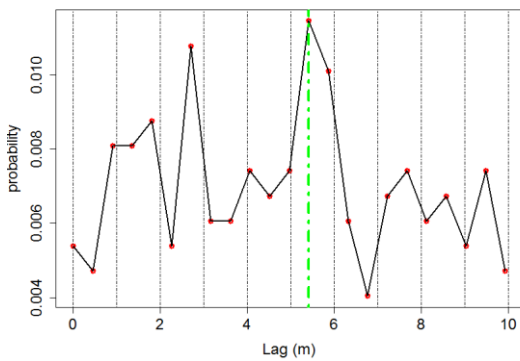
Subset	Average Crop rows spacing (m)		Row spacing difference between reference and detected (m)
	Reference	Detected	
1	2.68	2.71	0.03
Tuning	2.94	3.61	0.67
3	4.48	5.41	0.93
4	5.3	5.41	0.11



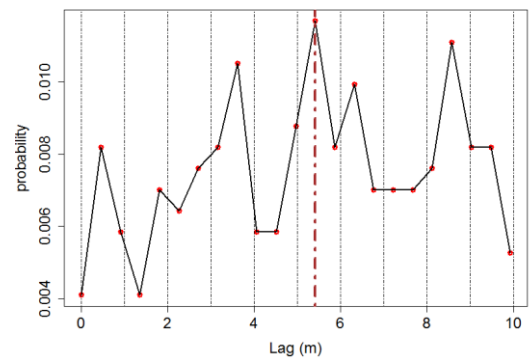
(a)



(b)



(c)



(d)

Figure 5.22: Row spacing of four subsets. (a) Subset 1, (b) tuning subset, (c) subset 3, (d) subset 4. The vertical lines indicate the lags at which dominant frequencies are found.

6. DISCUSSION

This thesis explored two real applications of LSD algorithm on agricultural sector: field boundary delineation and crop rows detection from satellite images. The results on field boundary delineation and crop rows detection are discussed in section 6.1 and section 6.2 respectively.

Linear features are extracted from remote sensing imagery using the LSD algorithm taking into account intensity differences between neighboring pixels. One of the most prominent advantages of remote sensing is the multispectral nature of the observations. However, the LSD algorithm takes only a single band as an input to detect linear segments. To make use of the advantage of the multispectral nature of the observations, the research proposes to combine all available information present in different bands as a single band before applying LSD algorithm. The LSD algorithm starts by calculating level-line angle for each pixel based on pixel gradient. Level-line angles are used to form line-support regions. Each line-support region is a potential candidate for a segment and is validated based on the calculation of a Number of False Alarms (NFA) of the corresponding geometrical event (rectangle) associated with it. In this research, all the eight bands of WorldView-2 image were used for field boundary delineation. Multispectral information was explored by taking the vector sum of gradients of all eight bands. For crop row detection panchromatic image band was used.

The automatically extracted line segments needed to be compared with the line segments in the reference dataset to check the performance of the algorithm. The validation method presented in this research is based on the method developed by Sidiropoulou Velidou et al. (2015), which uses the distance and orientation difference between the reference dataset and automatically extracted dataset. To assess the level of correspondence (correctness, completeness and positional accuracy) between the automatically detected line segments with the reference dataset and to estimate optimal values of the internal parameters of the LSD algorithm in the process of parameter tuning, two error ratios: ratio of missing detection (RM) and ratio of false detection (RF) were defined.

6.1. Field boundary delineation

The parameters tuned were scale S , gradient threshold ρ , angle tolerance τ and detection threshold ε . The optimal values of the three internal parameters obtained for this application were $S = 1.0$, $\tau = 22.5^\circ$ and $\varepsilon = 1.0$. The values of the two parameters τ and ε agreed with the ones proposed by Grompone von Gioi et al. (2012). Some difference was observed on the scale parameter. For this application, the value of S that minimized the sum errors $RM+RF$ with lower standard deviation is $S = 1.0$, whereas the one proposed by Grompone von Gioi et al. (2012) is $S = 0.8$.

The ratio of missing detection (RM) and the ratio of false detection (RF), defined in this validation method, have shown the general pattern of the results for different parameter values by providing quantitative measures and have been used for optimum parameter value selection. However, sometimes these measures were misleading, especially for extreme values of parameters. Visual inspection of results was necessary to ascertain whether these measures indeed reflect the optimum values or not.

The developed method is intended to detect all edges in an image by considering image intensity differences. To this end, even edges that do not represent field boundaries can be detected and give false detection for the purpose of this application. In the study area Mali, identifying edges that represent only

field boundaries from other features was a major problem. For example, the algorithm didn't make a distinction between edges that correspond to field boundaries and other edges formed due to the shadow of trees. Many line segments were extracted near trees in the field, which were actually not field boundaries. This led to an over detection of segments and in turn increased the number of false detections. Extracting trees from the image before detection could improve the detection results. On the other hand, the algorithm missed many edges. One possible cause for missing detection could be a weak contrast between neighboring fields.

In this research, an edge strength criterion was proposed to rank edges according to their strength. Two basic attributes of line segments: contrast and steepness were calculated for this purpose. For the automatically detected segments, edge strength analysis was performed using the developed criterion for both successful and false detections. It was observed that both average contrast and steepness of successful detections are higher than the corresponding values of false detections.

In this research, for the purpose of farm field boundary delineation, the LSD algorithm was tried on texture bands. Different second order GLCM texture measures were explored and results were analyzed. Studies have shown that incorporating texture measures could enhance the discrimination between spectrally similar classes (Blaschke, 2010). When land covers exhibit similar spectral characteristics and make classification difficult, the use of texture information is suggested as a potential solution (Lloyd et al., 2004). In this study, however, the use of GLCM texture measures could not improve the results.

6.2. Crop rows detection

After the tuning process, the optimum values of the internal parameters obtained for this application were $S = 0.8$, $\tau = 22.5^\circ$ and $\varepsilon = 1.0$. These optimum parameter values agree with the ones proposed by Grompone von Gioi et al. (2012). For these selected parameter values, the ratio of missing and the ratio of false detections are $RM = 0.17$ and $RF = 0.48$ respectively.

In this research, dominant orientation of crop rows was derived from the orientation of the automatically detected lines (or specifically from the gradient orientation of pixels) and comparison was made with the dominant orientations of reference dataset. The dominant orientations of crop rows of most of the subsets were identified correctly by the proposed method. The capability of the algorithm in detecting the spacing between the crop rows was also tested on four subsets of the image. The difference in row spacing between the reference and the automatically detected datasets ranged from 0.03 m to 0.93 m. One possible cause for this wide range could be the distribution of rows. Though most crop rows in a subset followed similar patterns and assumed to have the same spacing, there were some irregularities on the row spacing. This could have an effect on the automatically detected period (lag).

Accuracy assessment was conducted using the developed methodology to four subsets of the image. The results showed the occurrence of both false and missing detections. The results also revealed that RF is relatively higher than RM. One main cause for the occurrence of missing detection was the presence of trees in the field. Visual observation of the results has shown that most missing detections were observed for crop rows near trees. There were also changes in orientation of detected line segments for crop rows that were occluded by trees. The cause for high RF was related to the width of crop rows. Each crop row was represented by a single center line in the reference dataset. However, in most cases, the algorithm extracted more than one segment for wider crop rows. This led an increase in the number of detected crop rows (false detections). This problem could be minimized by adjusting the scale parameter, but could not be totally avoided.

7. CONCLUSIONS AND RECOMMENDATIONS

7.1. Optimal parameter setting

Parameter setting of the algorithm has great effect on the quality of the results produced. That is proper choice of parameter combination can lead to successful results. On the contrary, poor parameter setting may lead to unsatisfactory results. Therefore, finding the optimum values of parameters of the LSD algorithm that lead to successful detection of segments was an essential component of this study. The choice of the best set of parameter setting was performed using the developed methodology by minimizing the sum of errors of false and missing detections. In addition, visual inspection was performed to ascertain whether these measures indeed reflect the optimum values or not.

The three internal parameters of the algorithm involved in the tuning process were scale S , angle tolerance τ , and detection threshold ε . The scale parameter S involved in the algorithm helps to get a better representation of structure of certain features by controlling the spatial resolution of the image. The effect of the scale parameter on the detection results was very strong. Moreover, it controls the number of detected line segments. The number of detected line segments at low values of S was lower than the number at higher values of S for fixed values of other parameters. The second parameter tuned was angle tolerance τ . This parameter was related to region growing. Low τ values are more restrictive for region growing, which does not allow pixels with large differences in gradient orientation to be included in the same line-support region. The third parameter tuned was detection threshold. This parameter was responsible to distinguish ε -meaningful segments from all detected segments.

7.2. Assessment of the detection results

7.2.1. Field boundary delineation

The developed method for detecting field boundaries in areas with heterogeneous landscape was not as successful as expected. The different approaches followed: extracting information from multiple bands, using texture bands or image bands in detecting field boundaries do not give good results. Accuracy assessment was performed following the proposed method by defining the two error ratios: the ratio of missing detection and the ratio false detection. The results obtained for RM and RF were 0.78 and 0.73 respectively. The possible causes for these higher values of RM and RF were explored. The main cause for the high ratio of false detection was the presence of trees in the field. Many line segments were detected along the trees which didn't correspond to real field boundaries. One possible cause for missing detection could be a weak contrast between neighboring fields. Extracting trees and other irrelevant linear features like roads from the image before detection could improve the detection results. It is important to note that the algorithm was tested on a single scene of the study area. It may give different (better) results for less heterogeneous landscape.

7.2.2. Crop rows detection

Following the methodology for this application, the ratio of missing and the ratio of false detections on the image subset for which the parameter tuning was performed are 0.17 and 0.48 respectively. The capability of the algorithm in detecting the dominant orientation and the spacing between the crop rows was tested on four different subsets of the image. The algorithm identified the dominant orientation of crop rows correctly. From the tested four subsets, the maximum orientation difference between the reference and the detected crop rows was 2.87° which was observed on a single subset. But for the other

three subsets the orientation differences between the two datasets were within 0.57° , which shows the potential of the algorithm in detecting the dominant orientation of crop rows. The results of this research show that the adopted methodology has a good potential in detecting crop rows automatically from satellite images. However, it is important to note that the methodology was tested on different subsets of the same image but not on a different image. Moreover, it is better to compare the results of this algorithm to other standard methods that are used for automatic crop rows detection for detail analysis of the results.

7.3. Recommendations

The quality of the reference dataset has great influence on the end results as well as on the conclusions drawn from the results. The reference datasets in this research were digitized manually. Manual digitization of field boundaries and crop rows is error prone. It could have its own influence on the results. Therefore, whatever method applied, it is recommended to have accurate reference datasets. Moreover, knowledge of the study area assists on the decisions to be made. In this research, parameter tuning was performed by varying one parameter and keeping the others fixed. In future studies, it is recommended to develop a procedure to find the optimum values of the parameters automatically. The procedures followed in detecting the spacing between crop rows yielded reasonable results. These results could be improved by combining the procedure with other techniques present in literature such as Fast Fourier Transform. The region growing algorithm of the LSD is developed to detect straight linear features and rectangles are used for validation. The algorithm can be modified and applied according to the required shape to be detected.

LIST OF REFERENCES

- AGRA (2013). Africa Agriculture Status Reports. Retrieved August 24, 2015, from <http://agra-alliance.org/our-results/agra-status-reports/>
- Ali, Z. (2012). Assessing Usefulness of High-Resolution Satellite Imagery (HRSI) in GIS-based Cadastral Land Information System. *Journal of Settlements and Spatial Planning*, 3, 4.
- Ali, Z., Tuladhar, A., & Zevenbergen, J. (2012). An integrated approach for updating cadastral maps in Pakistan using satellite remote sensing data. *International Journal of Applied Earth Observation and Geoinformation*, 18, 386–398. <http://doi.org/10.1016/j.jag.2012.03.008>
- Arivazhagan, S., & Ganesan, L. (2003). Texture segmentation using wavelet transform. *Pattern Recognition Letters*, 24(16), 3197–3203. <http://doi.org/10.1016/j.patrec.2003.08.005>
- Barry, P., & Coakley, R. (2013). Field accuracy test of RPAS photogrammetry. *International Archives of the Photogrammetry, Remote Sensing and Spatial Information Sciences - ISPRS Archives*, 40(1W2), 27–31. Retrieved from <http://www.scopus.com/inward/record.url?eid=2-s2.0-84924227025&partnerID=tZOtx3y1>
- Bhardwaj, S., & Mittal, A. (2012). A Survey on Various Edge Detector Techniques. *Procedia Technology*, 4, 220–226. <http://doi.org/10.1016/j.protcy.2012.05.033>
- Blaschke, T. (2010). Object based image analysis for remote sensing. *5ISPRS6 Journal of Photogrammetry and Remote Sensing*, 65(1), 2–16. <http://doi.org/10.1016/j.isprsjprs.2009.06.004>
- Bogaerts, T., & Zevenbergen, J. (2001). Cadastral systems - alternatives. *Computers, Environment and Urban Systems*, 25, 325–337. [http://doi.org/10.1016/S0198-9715\(00\)00051-X](http://doi.org/10.1016/S0198-9715(00)00051-X)
- Burns, J. B., Hanson, A. R., & Riseman, E. M. (1986). Extracting Straight Lines. *IEEE Transactions on Pattern Analysis and Machine Intelligence*, PAMI-8(4), 425–455. <http://doi.org/10.1109/TPAMI.1986.4767808>
- Butenuth, M., Straub, M. B., & Heipke, C. (2004). Automatic extraction of field boundaries from aerial imagery. *KDNNet Symposium on Knowledge-Based Services for the Public Sector*, (pp. 3-4).
- Chang, D., Nesbitt, K. V., & Wilkins, K. (2007). The gestalt principles of similarity and proximity apply to both the haptic and visual grouping of elements. *Conferences in Research and Practice in Information Technology Series*, 64(C), 79–86. <http://doi.org/10.1109/WHC.2007.113>
- Da Costa, J. P., Michelet, F., Germain, C., Laviolle, O., & Grenier, G. (2007). Delineation of vine parcels by segmentation of high resolution remote sensed images. *Precision Agriculture*, 8(1-2), 95–110. <http://doi.org/10.1007/s11119-007-9031-3>
- Dale, P. F., & McLaughlin, J. D. (1988). *Land information management: an introduction with special reference to cadastral problems in Third World countries*. Clarendon Press. Retrieved from <http://books.google.com/books?id=MsDuAAAAMAAJ&pgis=1>
- Davis, L. S., Johns, S. A., & Aggarwal, J. K. (1979). Texture Analysis Using Generalized Cooccurrence Matrices, (3).
- Dekker, H. A. L. (2001). A new property regime in Kyrgyzstan; an investigation into the links between land reform, food security, and economic development. Retrieved from <http://www.narcis.nl/publication/RecordID/oai%3Auva.nl%3A254573>

- Desolneux, A., Moisan, L., & Morel, J. M. (2003). Computational gestalts and perception thresholds. *Journal of Physiology Paris*, 97(2-3), 311–324. <http://doi.org/10.1016/j.jphysparis.2003.09.006>
- Desolneux, A., Moisan, L., Morel, J.-M., 2008 . From Gestalt Theory to Image analysis. Vol.34. Springer New York.
- Donnelly, G. J. (2012). Fundamentals of Land Ownership, Land Boundaries, and Surveying. *Intergovernmental Committee on Surveying and Mapping*. Retrieved November 24, 2015. Retrieved from <http://www.icsm.gov.au/index.html>
- Evans, C., Jones, R., Svalbe, I., & Berman, M. (2002). Segmenting multispectral landsat TM images into field units. *IEEE Transactions on Geoscience and Remote Sensing*, 40(5), 1054–1064. <http://doi.org/10.1109/TGRS.2002.1010893>
- Faruquzzaman, a. B. M., Paiker, N. R., Arafat, J., Karim, Z., & Ali, M. A. (2008). Object segmentation based on split and merge algorithm. *IEEE Region 10 Annual International Conference, Proceedings/TENCON*, 2(2), 86–101. <http://doi.org/10.1109/TENCON.2008.4766802>
- Epifanio, I., & Soille, P. (2007). Morphological texture features for unsupervised and supervised segmentations of natural landscapes. *IEEE Transactions on Geoscience and Remote Sensing*, 45(4), 1074–1083. <http://doi.org/10.1109/TGRS.2006.890581>
- Ferencz, C., Bognár, P., Lichtenberger, J., Hamar, D., Tarcsai, G., Timár, G., ... Ferencz-Árkos, I. (2004). Crop yield estimation by satellite remote sensing. *International Journal of Remote Sensing*, 25(20), 4113–4149. <http://doi.org/10.1080/01431160410001698870>
- Franklin, S. E., Hall, R. J., Moskal, L. M., Maudie, A. J., & Lavigne, M. B. (2000). Incorporating texture into classification of forest species composition from airborne multispectral images. *International Journal of Remote Sensing*, 21(1), 61–79. <http://doi.org/10.1080/014311600210993>
- Grompone von Gioi, R., Jakubowicz, J., Morel, J.-M., & Randall, G. (2008). On Straight Line Segment Detection. *Journal of Mathematical Imaging and Vision*, 32(3), 313–347. <http://doi.org/10.1007/s10851-008-0102-5>
- Grompone von Gioi, R., Jakubowicz, J., Morel, J.-M., & Randall, G. (2012). LSD: a Line Segment Detector. *Image Processing On Line*, 2, 35–55. <http://doi.org/10.5201/ipol.2012.gjmr-lsd>
- Haralick, R. M., Shanmugam, K., & Dinstein, I. (1973). Textural Features for Image Classification. *IEEE Transactions on Systems, Man, and Cybernetics*, 3(6). <http://doi.org/10.1109/TSMC.1973.4309314>
- Harralick, R. M. (1979). Statistical and structural approach to texture. *Proceeding of IEEE*, 67(5), 786–804. <http://doi.org/10.1109/PROC.1979.11328>
- Harris, C., & Stephens, M. (1988). A Combined Corner and Edge Detector. *Proceedings of the Alvey Vision Conference 1988*, 147–151. <http://doi.org/10.5244/C.2.23>
- Heipke, C., Mayer, H., & Wiedemann, C. Evaluation of automatic road extraction. *LAPRS, "3D Reconstruction and Modeling of Topographic Objects."* Stuttgart, Vol. 32, September 17-19 1997
- Ishida, T., Itagaki, S., Sasaki, Y., & Ando, H. (2004). Application of wavelet transform for extracting edges of paddy fields from remotely sensed images. *International Journal of Remote Sensing*, 25(2), 347–357. <http://doi.org/10.1080/0143116031000115120>
- Jain, M., Mondal, P., DeFries, R. S., Small, C., & Galford, G. L. (2013). Mapping cropping intensity of smallholder farms: A comparison of methods using multiple sensors. *Remote Sensing of Environment*,

- 134, 210–223. <http://doi.org/10.1016/j.rse.2013.02.029>
- Janssen, L. L. F., & Molenaar, M. (1995). Terrain objects, their dynamics and their monitoring by the integration of GIS and remote sensing. *IEEE Transactions on Geoscience and Remote Sensing*, 33(3), 749–758. <http://doi.org/10.1109/36.387590>
- Ji, C. Y. (1996). Delineating agricultural field boundaries from TM imagery using dyadic wavelet transforms. *ISPRS Journal of Photogrammetry and Remote Sensing*, 16(95), 268–283.
- Jiang, H., Ngo, C., & Tan, H. (2006). Gestalt-based feature similarity measure in trademark database. *Pattern Recognition*, 39(August 2005), 1–35. <http://doi.org/10.1016/j.patcog.2005.08.012>
- Jing, Y., Zevenbergen, J. & Ma, Z. (2011). Assessing Larsi-Integrated Participation Procedure for Urban Adjudication in China, (May 18-22), 105. Retrieved from http://www.itc.nl/library/papers_2011/msc/la/jing.pdf
- Kurwakumire, E. (2014). Digital Cadastres Facilitating Land Information Management. *South African Journal of Geomatics*, 3(1), 64–77.
- Lengoiboni, M., van der Molen, P., & Bregt, A. K. (2011). Pastoralism within the cadastral system: Seasonal interactions and access agreements between pastoralists and non-pastoralists in Northern Kenya. *Journal of Arid Environments*, 75(5), 477–486. <http://doi.org/10.1016/j.jaridenv.2010.12.011>
- Lloyd, C. D., Berberoglu, S., Curran, P. J., & Atkinson, P. M. (2004). A comparison of texture measures for the per-field classification of Mediterranean land cover. *International Journal of Remote Sensing*, 25(19), 3943–3965. <http://doi.org/10.1080/0143116042000192321>
- Lin, Y., Wang, C., Cheng, J., Chen, B., Jia, F., Chen, Z., & Li, J. (2015). Line segment extraction for large scale unorganized point clouds. *ISPRS Journal of Photogrammetry and Remote Sensing*, 102, 172–183. <http://doi.org/10.1016/j.isprsjprs.2014.12.027>
- Meer, P., & Georgescu, B. (2001). Edge detection with embedded confidence. *IEEE Transactions on Pattern Analysis and Machine Intelligence*, 23(12), 1351–1365. <http://doi.org/10.1109/34.977560>
- Min, H. (2015). A Novel Level Set Model Based on Multi-scale Local Structure Operation for Texture Image Segmentation. *Journal of Information and Computational Science*, 12(1), 9–20. <http://doi.org/10.12733/jics20105180>
- Moisan, L., & Morel, J.-M. (2000). Meaningful Alignments Agnes Desolneux. *International Journal of Computer Vision*, 40(1), 7–23. <http://doi.org/10.1.1.28.885>
- Morel, J., Randall, G., & Gioi, R. G. Von. (2010). LSD : A Fast Line Segment Detector with a False Detection Control, 32(4), 722–732.
- Mueller, M., Segl, K., & Kaufmann, H. (2004). Edge- and region-based segmentation technique for the extraction of large, man-made objects in high-resolution satellite imagery. *Pattern Recognition*, 37(8), 1619–1628. <http://doi.org/10.1016/j.patcog.2004.03.001>
- Nixon, M., & Aguado, A. (2012). Feature Extraction & Image Processing for Computer Vision, Third Edition. In *Feature Extraction & Image Processing for Computer Vision, Second Edition*. <http://doi.org/10.1016/B978-0-12-396549-3.00003-3>
- Officers, A. (2012). Standard on Digital Cadastral Maps and Parcel Identifiers, (January), 1–18.
- Pearsall, J. (1998). *The New Oxford Dictionary of English*. Oxford: Oxford University Press.
- Rutzinger, M., Rottensteiner, F., & Pfeifer, N. (2009). Extraction From Airborne Laser Scanning. *Ieee*

Journal of Selected Topics in Applied Earth Observations and Remote Sensing, 2(1), 11–20.

- Rydberg, A., Borgefors, G., & Member, S. (2001). Integrated Method for Boundary Delineation of Agricultural Fields in Multispectral Satellite Images. *IEEE Transactions on Geoscience and Remote Sensing*, 39(11), 2514–2520.
- Ryherd, S., & Woodcock, C. (1996). Combining Spectral and Texture Data in the Segmentation of Remotely Sensed Images. *Photogrammetric Engineering Remote Sensing*, 62(2), 181–194. Retrieved from http://www.asprs.org/publications/pers/96journal/february/1996_feb_181-194.pdf
- Sainz-Costa, N., Ribeiro, A., Burgos-Artizzu, X. P., Guijarro, M., & Pajares, G. (2011). Mapping wide row crops with video sequences acquired from a tractor moving at treatment speed. *Sensors*, 11(7), 7095–7109. <http://doi.org/10.3390/s110707095>
- Sarkar, S., & Boyer, K. L. (1993). Perceptual organization in computer vision: a review and a proposal for classifier extractor. *IEEE Transactions on Systems, Man, and Cybernetics*, 23(2), 382–399.
- Sidiropoulou Velidou, D., Tolpekin, V. A., Stein, A., & Woldai, T. (2015). Use of Gestalt Theory and Random Sets for Automatic Detection of Linear Geological Features. *Mathematical Geosciences*, 47(3), 249–276. <http://doi.org/10.1007/s11004-015-9584-z>
- STARS Project, June 24–26, 2015, STARS general meeting, ITC, Enschede. Personal communication.
- Tepper, M., Musé, P., Almansa, A., & Mejail, M. (2014). Finding contrasted and regular edges by a contrario detection of periodic subsequences. *Pattern Recognition*, 47(1), 72–79. <http://doi.org/10.1016/j.patcog.2013.06.025>
- Tiwari, P. S., Pande, H., Kumar, M., & Dadhwal, V. K. (2009). Potential of IRS P-6 LISS IV for agriculture field boundary delineation. *Journal of Applied Remote Sensing*, 3(1), 033528. <http://doi.org/10.1117/1.3133306>
- Torre, M., & Radeva, P. (2000). Agricultural-field extraction on aerial images by regioncompetition algorithm. *Proceedings 15th International Conference on Pattern Recognition. ICPR-2000*, 1. <http://doi.org/10.1109/ICPR.2000.905337>
- Turker, M., & Kok, E. H. (2013). Field-based sub-boundary extraction from remote sensing imagery using perceptual grouping. *ISPRS Journal of Photogrammetry and Remote Sensing*, 79, 106–121. <http://doi.org/10.1016/j.isprs.2013.02.009>
- Ursani, A. A., Kpalma, K., Lelong, C. C. D., & Ronsin, J. (2012). Fusion of textural and spectral information for tree crop and other agricultural cover mapping with very-high resolution satellite images. *IEEE Journal of Selected Topics in Applied Earth Observations and Remote Sensing*, 5(1), 225–235. <http://doi.org/10.1109/JSTARS.2011.2170289>
- Williamson, I., & Ting, L. (2001). Land administration and cadastral trends - A framework for re-engineering. *Computers, Environment and Urban Systems*, 25(4-5), 339–366. [http://doi.org/10.1016/S0198-9715\(00\)00053-3](http://doi.org/10.1016/S0198-9715(00)00053-3)
- Yan, L., & Roy, D. P. (2014). Automated crop field extraction from multi-temporal Web Enabled Landsat Data. *Remote Sensing of Environment*, 144, 42–64. <http://doi.org/10.1016/j.rse.2014.01.006>
- Yuan, J., & Cheriyyadat, A. M. (2014, November). Learning to count buildings in diverse aerial scenes. In *Proceedings of the 22nd ACM SIGSPATIAL International Conference on Advances in Geographic Information Systems* (pp. 271–280). ACM.

Ziou, D., & Tabbone, S. (1998). Edge detection techniques - An overview. *International Journal of Pattern Recognition and Image Analysis*, 8(4), 1–41.

APPENDIX

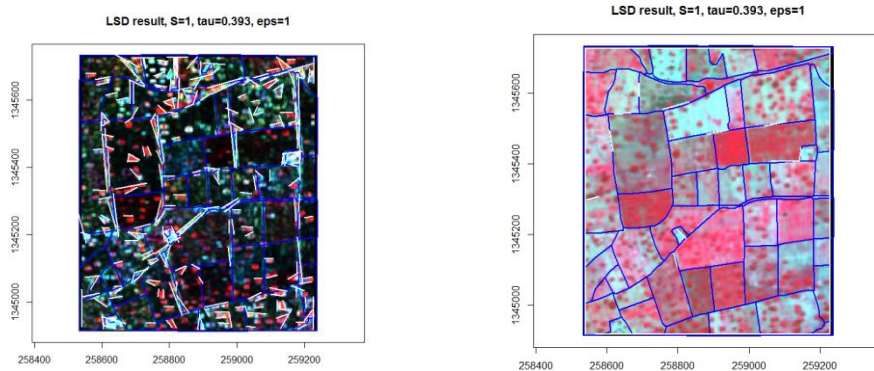
A. LSD results

```
> LSD_results
```

	length	width	angle	NFA	x_start	y_start	x_end	y_end	contrast	steepness
32	117.52538	18.041200	6.16869403	7.525482e-61	258599.8	1345548	258616.6	1345430	0.0098674492	5.469397e-04
18	134.30694	13.188099	4.66916689	4.488808e-58	259004.4	1345401	259139.5	1345408	0.0256514769	1.945047e-03
94	100.69742	6.162088	6.18368839	2.210375e-56	258986.8	1345503	259000.8	1345403	0.0099082805	1.607942e-03
27	153.47818	27.475311	4.34249428	6.952355e-55	259088.2	1345685	259236.0	1345713	0.0031590496	1.149778e-04
74	118.05106	17.975575	4.50813418	8.157291e-52	258931.0	1344998	259049.6	1345012	0.0169705425	9.440890e-04
36	99.98311	16.208968	6.27916420	7.580948e-50	258693.7	1345661	258690.4	1345560	0.0117696309	7.261185e-04
180	72.80196	12.920924	6.19043014	5.291193e-47	259164.1	1345673	259175.5	1345600	0.0126527486	9.792448e-04
181	72.42593	15.767758	0.05256066	2.604288e-45	258856.1	1345374	258852.5	1345301	0.0117795848	7.470678e-04
190	116.81611	10.940749	6.18403681	5.739770e-44	259220.2	1345430	259230.8	1345312	0.0037490608	3.426695e-04
92	96.51885	4.924835	6.17591808	1.235488e-43	258993.3	1345498	259004.7	1345401	0.0225380491	4.576407e-03
13	279.55582	38.535965	4.40232378	1.396334e-43	258694.3	1345539	258964.2	1345616	0.0056918750	1.477029e-04
20	108.82283	15.519091	4.37749510	4.115675e-42	258636.4	1345320	258537.9	1345303	0.0067614380	4.356852e-04
78	93.85275	14.761546	4.75099750	7.613089e-42	258778.8	1345276	258873.5	1345272	0.0067734392	4.588570e-04
118	53.97346	8.434928	0.03135225	3.418508e-39	258803.2	1345727	258800.1	1345673	0.0088442381	1.048526e-03
138	48.58762	13.326749	4.97822437	7.751598e-39	259185.4	1345241	259234.9	1345234	0.0117784621	8.838211e-04
38	50.03584	11.666301	4.65954019	2.242716e-34	258938.3	1344954	258989.6	1344951	0.0103931355	8.908681e-04
59	41.51078	25.390886	5.74008763	3.255781e-32	258883.0	1344954	258902.6	1344916	0.0277128109	1.091447e-03
98	125.77036	15.786539	6.01688523	7.605895e-32	258807.6	1345101	258838.1	1344978	0.0079386754	5.028762e-04
53	40.85431	21.692226	5.73615658	3.638376e-30	259137.6	1345006	259161.9	1344972	0.0221678859	0.021928e-03
101	76.41153	23.112074	4.59272206	9.587505e-30	258962.0	1345717	259039.6	1345721	0.0128490115	5.559437e-04
15	89.38073	13.299541	4.56976816	1.557665e-29	259006.2	1345645	259095.2	1345661	0.0174115513	1.309184e-03
159	38.38955	7.093583	4.62077985	1.050884e-28	259194.6	1345184	259233.7	1345189	0.0079041970	1.114274e-03
19	47.98296	10.757725	4.48155015	1.492777e-28	258538.7	1345202	258584.5	1345221	0.0204344483	1.900351e-03
51	60.05299	14.266947	4.72730648	6.697155e-28	258538.4	1345536	258599.5	1345536	0.0126769872	8.885564e-04
113	70.19661	11.779519	6.23903421	5.495732e-27	258779.0	1345392	258779.1	1345320	0.0082608318	7.012877e-04
58	58.73647	12.818117	5.97488679	1.488279e-26	258784.6	1345156	258801.0	1345099	0.0244723965	1.909204e-03
158	37.31430	13.041224	4.49254888	1.712946e-26	258806.4	1345099	258844.3	1345105	0.0011595520	8.891435e-05
7	142.80922	21.627201	4.56482209	1.196574e-25	258559.8	1345206	258704.5	1345210	0.0164440018	7.603389e-04
84	75.23362	14.152649	4.57123564	3.489949e-25	258902.4	1345488	258977.6	1345500	0.0273847185	1.934953e-03
77	61.97870	22.728359	6.08675044	5.223883e-25	258752.5	1345551	258768.6	1345490	0.0111618468	4.910978e-04
54	58.03728	8.240885	4.72244288	5.679364e-25	258888.5	1344918	258832.5	1344927	0.0025889644	3.141610e-04
34	80.47828	17.979131	4.46195368	6.407905e-25	259034.3	1345002	259114.2	1345018	0.0053214942	2.959817e-04
42	73.02022	16.511813	4.02429018	2.061652e-24	258748.2	1345226	258687.7	1345199	0.0141101412	8.545483e-04
66	113.79396	17.781432	4.59634748	2.097452e-24	258983.6	1345289	259097.7	1345301	0.0115876277	6.516701e-04
49	37.94569	12.092624	4.39994156	9.913254e-23	259002.8	1345658	259038.8	1345673	0.0194680393	1.609910e-03
28	46.55851	9.565656	4.61540034	2.118481e-22	259186.4	1345434	259233.5	1345441	0.0091410559	9.556120e-04
40	43.77027	9.613072	5.92551440	2.240960e-22	259059.0	1345357	259076.1	1345315	0.0106709808	1.110049e-03
144	36.87412	9.858612	6.07935419	3.589580e-22	259016.6	1345095	259023.5	1345058	0.0104521786	1.060208e-03
145	58.81909	10.864967	5.01385842	4.177690e-22	258702.9	1345660	258757.2	1345634	0.0215742930	1.985675e-03
69	54.76258	12.575119	4.78932421	7.269014e-22	258601.9	1345543	258657.7	1345541	0.0129395821	1.028983e-03
128	24.31722	11.497501	4.77252610	7.637028e-22	258852.3	1345386	258877.5	1345383	0.0167345241	1.455492e-03
80	48.02223	19.041587	6.21310850	9.352244e-22	259188.8	1345500	259184.5	1345450	0.0152462235	8.006803e-04
1	40.18441	16.421682	4.58531945	2.277145e-21	259146.9	1345446	259189.0	1345441	0.0328853282	2.002555e-03
61	58.72742	23.162704	4.28957253	2.366595e-21	258678.9	1345536	258728.9	1345570	0.0113696915	4.908620e-04
155	22.78348	11.434691	0.30816786	5.038339e-21	259134.0	1345400	259118.6	1345380	0.0108090360	9.452845e-04
64	48.29739	10.163242	0.06823605	1.038368e-20	259187.5	1345062	259201.4	1345101	0.0048914257	4.812860e-04
137	32.80149	11.298855	4.06430580	1.043676e-20	259108.9	1345628	259135.5	1345649	0.0166995503	1.477986e-03
135	49.66811	8.437279	4.03340934	1.112490e-20	258710.0	1345079	258749.0	1345112	0.0269528563	3.194496e-03
6	23.96061	17.378550	0.29612869	1.167189e-20	258626.5	1344952	258604.6	1344936	0.0144898888	8.337801e-04
123	44.34315	9.590148	4.66268103	2.196980e-20	258990.6	1345168	259017.3	1345180	0.0148595789	1.549463e-03
184	54.89448	20.763028	0.54855766	3.873301e-20	259173.8	1345138	259136.6	1345095	0.0138647075	6.677594e-04
173	72.24955	17.769519	6.19941034	4.336373e-20	258812.8	1345727	258820.5	1345654	0.0088926663	5.004450e-04

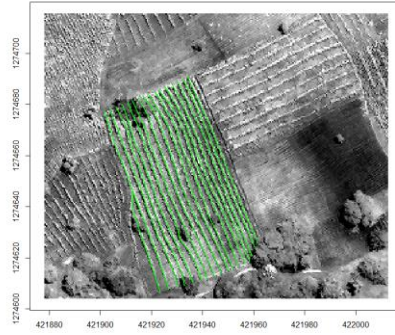
Snapshot of LSD results showing different attributes: length, width, angle, NFA, end points of lines, contrast and steepness.

B. LSD results on texture bands



(a) GLCM contrast for $d=3$ (b) GLCM mean for $d=3$. Only a few segments were detected.

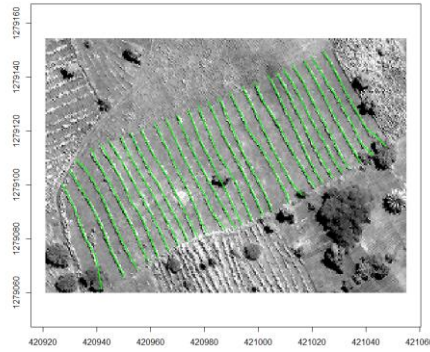
C. Reference dataset for crop rows of different subsets.



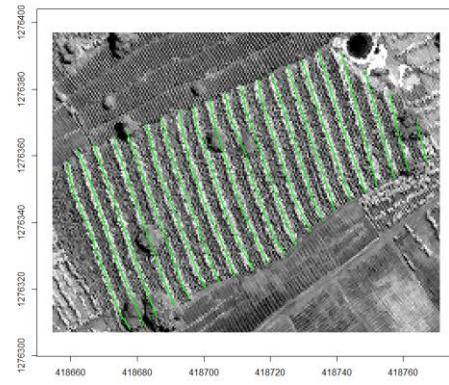
(a) Subset1



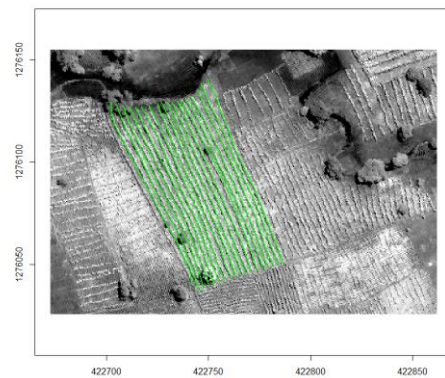
(b) subset 2



(c) Subset 3



(d) Subset 4



(e) Tuning subset